

# SASNet: Spatially-Adaptive Sinusoidal Neural Networks

Haoan Feng<sup>1</sup>, Diana Aldana<sup>2</sup>, Tiago Novello<sup>2</sup>, Leila De Floriani<sup>1</sup>  
<sup>1</sup>University of Maryland, College Park, <sup>2</sup> IMPA

hfengac@umd.edu, diana.aldana@impa.br,  
 tiago.novello@impa.br, deflo@umd.edu

## Abstract

Sinusoidal neural networks (SNNs) have emerged as powerful implicit neural representations (INRs) for low-dimensional signals in computer vision and graphics. They enable high-frequency signal reconstruction and smooth manifold modeling; however, they often suffer from spectral bias, training instability, and overfitting. To address these challenges, we propose SASNet, Spatially-Adaptive SNNs that robustly enhance the capacity of compact INRs to fit detailed signals. SASNet integrates a **frequency embedding layer** to control frequency components and mitigate spectral bias, along with jointly optimized, **spatially-adaptive masks** that localize neuron influence, reducing network redundancy and improving convergence stability. Robust to hyperparameter selection, SASNet faithfully reconstructs high-frequency signals without overfitting low-frequency regions. Our experiments show that SASNet outperforms state-of-the-art INRs, achieving strong fitting accuracy, super-resolution capability, and noise suppression, without sacrificing model compactness.

## 1. Introduction

Implicit neural representations (INRs) have gained prominence as powerful tools for representing low-dimensional signals in a variety of vision-related tasks, including image synthesis [12, 26], 3D shape reconstruction [16, 32], and scene representation [9, 17, 31]. INRs encode input data implicitly as neural network weights by mapping spatial coordinates directly to scalar values. Among INRs, sinusoidal neural networks (SNNs), which employ the sine function as activation function, have attracted significant attention due to their ability to capture high-frequency signal details and model function derivatives at the same time [32]. Consequently, SNNs provide an implicit smooth representation of the input signal, making SNNs effective for function modeling and analysis of scalar field manifolds [7].

However, the signal reconstruction quality of SNNs re-

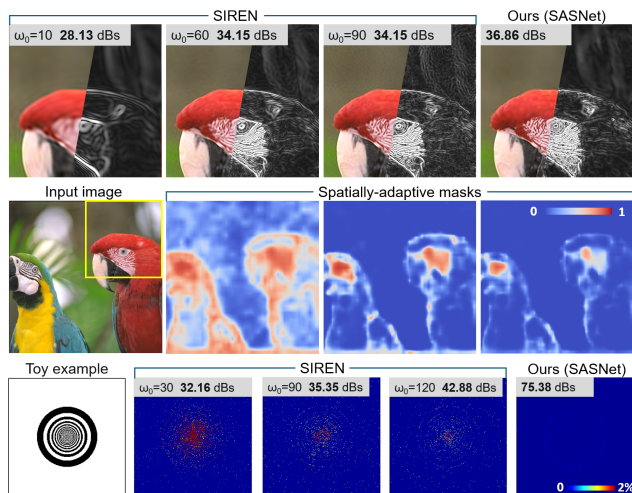


Figure 1. We present **SASNet**, a robust INR that allows training SNNs with spatial localization overcoming challenges in frequency initialization, hyperparameter selection, and noisy reconstruction. First row compares, on a  $\times 16$  super-resolution, SIREN [32] with different hyperparameter  $\omega_0$ 's and our SASNet. As illustrated in the first three images, *blurriness*, “ringing” around edges, and *noisy background* are common artifacts. Second row presents three jointly optimized spatially-adaptive masks for different frequency bands (low to high). As a toy example, last row shows fitting error maps of SIREN with different  $\omega_0$ 's and of SASNet under the same color encoding (up to 2% absolute difference).

mains limited by the *spectral bias* and the initialization of frequency hyperparameters  $\omega_0$ 's [35]. As shown in Fig. 1, SNNs are highly sensitive to the choice of  $\omega_0$ , often leading to visual artifacts such as *blurriness*, “ringing” around edges (due to missing high-frequency signal components), and *noisy backgrounds*. A small  $\omega_0$  yields an image with a clean background but a blurry reconstruction in high-frequency regions (e.g., edges and textures), while a large  $\omega_0$  introduces noise but enhances image details. These limitations significantly restrict the practical applications of such INRs. Furthermore, increasing the training steps to

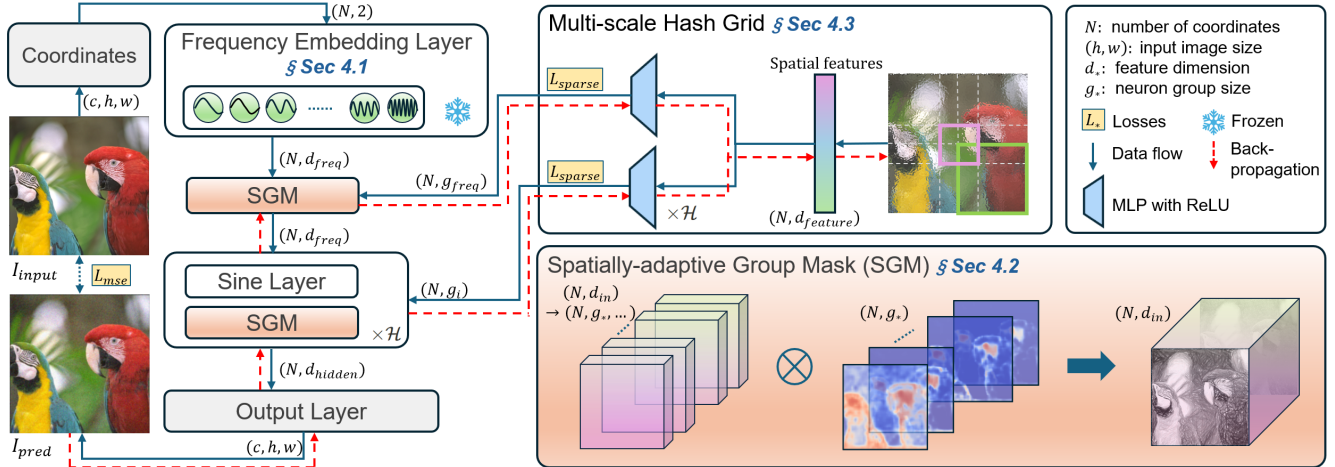


Figure 2. **Overview of SASNet.** A multi-scale hash grid is constructed to interpolate spatial features that are decoded to spatially-adaptive group masks (SGMs) for layers in the SNN. A mask is applied to a group of neurons via broadcasting and Hadamard product. The frequency embedding layer is initialized and frozen after the network construction stage. Our network contains  $\mathcal{H}$  hidden *Sine Layers* following the design in SIREN [32]. Training data flow and back-propagation paths are highlighted as in the legend.

restore high-frequency details can lead to unstable training and overfitting, leading to poor generalization and inaccurate reconstruction of signal derivatives. Since coordinates are treated independently by SNNs, neurons contributing to the high-frequency regions often propagate to smoother regions as noise (overfitting), leading to noisy reconstruction and waste of models’ fitting capacity.

To overcome these challenges, we introduce **SASNet** (Spatially-Adaptive Sinusoidal Neural Network) that allows robust frequency control and makes the SNN weights spatially dependent, resulting in *frequency localization*. SASNet uses a novel *frequency embedding layer* to enable precise control over the frequency components. During training, *spatially-adaptive masks* are jointly optimized to regulate the influence of different frequency bands and constrain each neuron to specific domain regions (see Fig. 1, second row). As a result, network redundancy and overfitting are alleviated, allowing the network to utilize its capacity more efficiently. This not only stabilizes the training process of an SNN but also enhances its ability to capture high-frequency details and mitigates overfitting artifacts at the same time. Our main contributions are threefold:

- **Frequency embedding layer:** It enables control over SNN frequency components and adaptive localization, improving reconstruction of high-frequency regions.
- **Jointly optimized spatially-adaptive masks:** Based on a lightweight multi-scale hash grid, masks are jointly optimized to control the localization of different frequency bands. This minimizes overfitting in smooth regions, reduces SNN redundancy, and increases INR capacity.
- **Robust training and faster convergence:** SASNet mitigates the interference of high-frequency neurons in do-

main regions with lower frequencies. This leads to more stable training and faster convergence than other methods (see Fig. 5), enhancing convergence even after many training steps — a common challenge in training INRs.

## 2. Related work

Implicit neural representations (INRs) have become foundational tools in computer vision and graphics for modeling complex signals. SNNs are a special class of INRs that parameterize signals continuously, offering several advantages, including memory efficiency, parallel inference, differentiability, and the ability to capture fine-grained details [5]. XINC [20] proposes to analyze the *contribution map* of each neuron in INRs to effectively understand the network fitting capability and behaviors. Based on the contribution map, INRs can be classified into three groups: *Global*, *Local*, and *Hybrid* representations (see Fig. 3).

### 2.1. Global neural representations

In global INRs, each neuron contributes to the entire spatial domain. Early works include ReLU-based MLPs, which exhibit spectral bias - favoring low-frequency components and struggling to model high-frequency details [23, 25]. To address this limitation, FFN [33] introduces positional encoding to enable MLPs to capture high-frequency variations. Alternative activation functions, such as sine [32], Gaussian [24], and sinc [29] functions, have also been explored to alleviate spectral bias and improve fitting accuracy. Additionally, BACON [13] adopts the shallow multiplicative network design from MFN [6] to control output frequencies and achieve adaptive band-limit control. However, this design sacrifices the network compactness com-

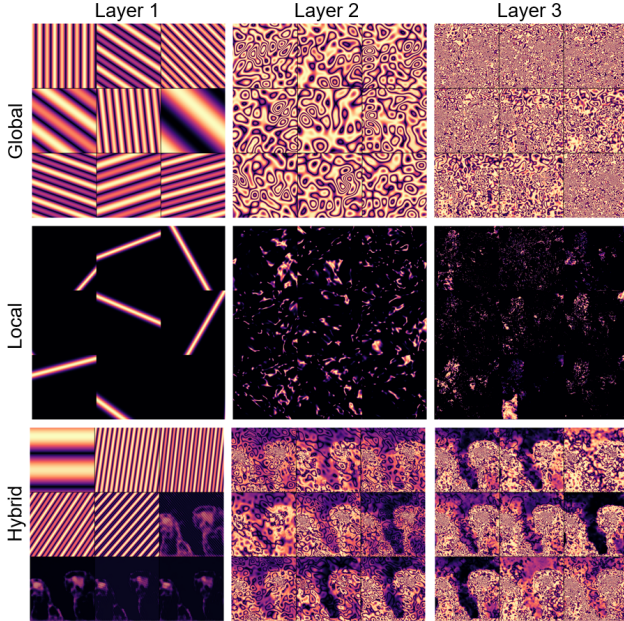


Figure 3. Neurons’ contribution maps of different INRs for the image in Fig. 1. From left to right, each column shows 9 selected maps from hidden layers of each INR. *Zoom in to visualize details.*

pared to MLPs, as evidenced in Theorem 1.

SNNs effectively model high-frequency details while maintaining smooth manifold regularization [32]. However, they are difficult to train [21]. SIREN [32] resolves this with a dedicated initialization scheme that allows training SNNs and ensures convergence. Recently, Novello et al. [19] propose explicit frequency control and network weights bounding strategies to enhance SNNs’ representation capabilities and reduce model overfitting. FINER [14] introduces a dynamic scale factor for increasing frequency by modifying the activation function, enabling the model to fit a broader range of signal frequencies. However, it requires a careful bias initialization, potentially causing unstable training. Shi et al. [30] mitigate MLP spectral bias via weight reparameterization with a Fourier basis, while Mehta et al. [15] and Kazerouni et al. [10] enhance SIREN’s frequency range via adding additional network branches.

Despite their compactness and expressiveness, global neural representations face challenges due to their global contribution. This characteristic limits their function modeling capacity and parameter efficiency, often leading to blurriness and noisy background, as illustrated in Fig. 1.

## 2.2. Local neural representations

Local INRs restrict the influence of neurons to specific regions of the domain, enhancing model scalability and enabling better modeling of localized variations. Examples include using the sinc function as activation [29] and

WIRE [28], which employ complex Gabor wavelets as activations. By leveraging the locality of wavelets, WIRE efficiently represents high-frequency signals; however, this design poses challenges in the hyperparameter initialization and increases the risk of overfitting and unstable training.

Inspired by the success of Gaussian splatting [11], the research community has investigated the use of 2D Gaussian kernels for image fitting. GaussianImage [38] enhances inference efficiency and reduces model size by leveraging Cholesky decomposition, streamlining the rasterization pipeline, and compressing model parameters. Meanwhile, Image-GS [39] introduces a tailored gradient-based initialization along with a pruning-and-densification strategy specifically designed for image fitting.

Though avoiding the shortcoming of global representations, local representations often suffer from overfitting and no explicit band limit control, leading to inaccurate sub-pixel values and bad generalization capability. Additionally, local representations usually require more parameters than global ones, limiting the model’s parameter efficiency.

## 2.3. Hybrid neural representations

Hybrid neural representations seek the best of both worlds from global and local methods. Hybrid methods typically decompose the spatial domain into sub-regions or leverage multi-scale features to simultaneously capture global structures and local details. NeRF [17] and InstantNGP [18] employ ray tracing and multi-scale feature concatenation to represent 3D scenes implicitly in network weights. However, these approaches often require a large number of parameters and computationally intensive training.

MINER [27] decomposes the domain into multi-level tiles, iteratively fitting the residual from previous tiers using independent SIRENs. Instead of learning local frequency representations, NeuRBF [4] combines fixed frequency embeddings with radial basis functions (RBFs) and employs a dedicated spatial domain decomposition. By carefully initializing centers and scales of RBFs, each query coordinate interpolates frequency-embedded features from its nearest RBFs before being processed by an MLP. While effective, these methods still suffer from severe overfitting and reduced expressiveness, especially when constrained to a small model size. To alleviate the overfitting in FFN [33], SAPE [8] employs a progressive fitting strategy with a residual-dependent local mask, incrementally increasing model capacity and introducing high-frequency embeddings in poorly reconstructed regions. SAPE relies on a single-mask with update policy and is constrained by positional embedding design for optimal fitting quality. However, like FFN, the ReLU activation function applied harms the signal derivative accuracy.

Our SASNet also falls into this hybrid category. Harvesting strengths of both worlds, it greatly reduces overfitting in

smooth regions, enables faster convergence, and achieves better reconstruction quality with a compact model.

### 3. Method

We introduce SASNet, a model designed to mitigate overfitting and enhance the parameter efficiency of SNNs. It consists of a frequency embedding layer (Sec. 3.1), spatially-adaptive masks (Sec. 3.2), and a network design that jointly optimizes masks via a multi-scale hash grid (Sec. 3.3).

A SNN is a *multilayer perceptron* (MLP) that employs the *sine* function as its activation. An SNN  $f$  of *depth*  $d \in \mathbb{N}$  is constructed by composing  $d$  *sinusoidal layers* with an affine transformation. The first layer maps input coordinates to a harmonic representation of the form  $\sin(\omega \mathbf{x} + \varphi)$ . Inspired by the Fourier series, we refer to  $\omega$  and  $\varphi$  as the *input frequencies* and *phase shifts*. SNNs demonstrated high representational capacity even with a shallow architecture [22, 32, 37], where sinusoidal layers play a fundamental role in function representation [19, 36].

The  $ij$ -neuron  $h_j^i(\mathbf{x})$  of a network refers to the  $j$ -th neuron of the  $i$ -th layer, represented by  $\mathbf{h}^i(\mathbf{x})$ , which is the composition of the first  $i$  layers. Precisely,

$$h_j^{i+1}(\mathbf{x}) = \sin \left( \sum_{k=1}^n W_{jk}^{i+1} \underbrace{\sin(\mathbf{y}_k^i)}_{h_k^i(\mathbf{x})} + b_j^{i+1} \right), \quad (1)$$

where  $\mathbf{y}^i$  denotes the linear transformation of  $\mathbf{h}^i(\mathbf{x})$ , and  $W$  and  $b$  represent the weight matrix and bias, respectively. Consequently, the weight  $W_{jk}^{i+1}$  determines the influence of neuron  $h_k^i$  in shaping the next layer. Novello et al. [19] shows that a hidden neuron (1) can be expanded as follows:

**Thrm 1** *The neuron  $h_j^{i+1}$  has the following expansion:*

$$h_j^{i+1}(\mathbf{x}) = \sum_{\mathbf{k} \in \mathbb{Z}^n} \alpha \sin \left( \langle \mathbf{k}, \mathbf{y} \rangle + b_j^{i+1} \right), \quad (2)$$

with amplitudes  $\alpha$  given by the product  $\alpha = \prod_l J_{k_l}(W_{jl}^{i+1})$  of Bessel functions of the first kind that evaluated at  $W_{jl}^{i+1}$ .

Theorem 1 shows that SNNs generate frequencies as integer combinations  $\langle \mathbf{k}, \omega \rangle$  of the input frequencies  $\omega$ . This enables the model to fit more frequency components with less parameters, resulting in a compact representation. In Sec. 3.1, we leverage this to design an initialization scheme for controlling the network’s band limit. Moreover, the weight matrices  $\mathbf{W}^i$  determine the amplitude  $\alpha$  of each generated frequency, which is independent of spatial coordinates  $\mathbf{x}$ . Thereby, it can introduce high-frequency noise into smooth regions. To mitigate this artifact, Sec. 3.2 introduces *spatially-adaptive masks* to make the amplitude spatially dependent,  $\alpha_{mask} = \alpha \cdot \text{mask}(\mathbf{x})$ , ensuring that different frequencies localize to appropriate domain regions.

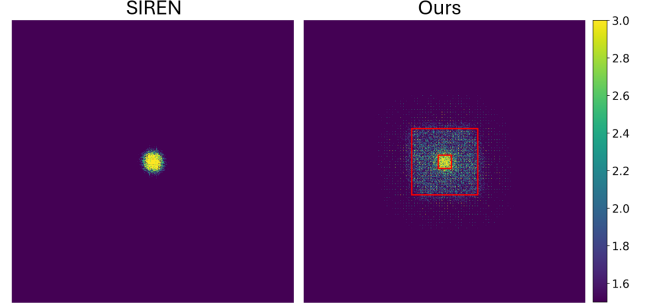


Figure 4. Comparing the frequency spectra of SIREN and our SASNet before training. Two red rectangles indicate band limits of low- and high-frequency embedding neurons.

#### 3.1. Frequency embedding layer

By Theorem 1, the frequencies generated by an SNN are fully determined by the first-layer weights  $\omega$ . Proper initialization of  $\omega$  thus accelerates convergence and mitigates spectral bias [19]. We propose an initialization scheme that partitions  $\omega$  into low- and high-frequency groups, forming a *frequency embedding layer* that remains fixed during training. To ensure consistency with Fourier series expansion, all neuron frequencies are initialized as integer multiples of the lowest *basis frequency* of the signal, defined as  $\frac{2\pi}{P}$ , where  $P$  denotes the period (e.g.,  $P = 2$  for networks operating on coordinates within  $[-1, 1]$ ).

As shown in Fig. 4, given a predefined band limit  $\mathcal{B}$  and a low-frequency range  $\mathcal{L}$ , we split the frequency domain for selecting  $\omega$  into two concentric rectangular regions giving rise to the low- and high-frequency neurons. Considering image-fitting as an example, low-frequency neuron multipliers  $\mathbf{k}_{low} \in \mathbb{Z}^2$  are randomly sampled from  $[-\mathcal{L}, \mathcal{L}]^2$ . To ensure better coverage, high-frequency multipliers  $\mathbf{k}_{high}$  are sampled on an integer grid within  $[-\mathcal{B}, \mathcal{B}]^2$ , excluding the low-frequency region  $[-\mathcal{L}, \mathcal{L}]^2$ . To reduce redundancy, we constrain sampling to positive integers along the  $x$ -axis, leveraging a symmetry of the frequency domain, where  $(k_x, -k_y)$  is equivalent to  $(-k_x, k_y)$ . By adjusting  $\mathcal{B}$  and balancing low- and high-frequency neurons, SASNet explicitly controls the output frequencies, improving high-frequency detail reconstruction. Choosing an appropriate  $\mathcal{B}$  mitigates overfitting and enhances the reconstruction of high-frequency details.

The initialization of the remaining network weights follows the standard SIREN [32] scheme. Unlike SIREN, where all frequencies evolve during training, our method ensures a fixed frequency structure, resulting in a faster convergence and more stable training as shown in Fig. 5.

#### 3.2. Spatially-adaptive masks

As discussed in Sec. 2, allowing neurons to have global contribution maps may lead to overfitting on low-frequency re-

gions and parameter redundancy. To overcome this, we propose spatially-adaptive masks, which help in localizing neuron contributions maps. Precisely, for each  $ij$ -neuron  $h_j^i$ , we apply a mask  $\mathcal{M}_j^i(\mathbf{x}) \in [0, 1]$  to adjust its influence over the domain. In other words, the  $i$ -th layer  $\mathbf{h}^i$  is replaced by  $\tilde{\mathbf{h}}^i(\mathbf{x}) = \mathcal{M}^i(\mathbf{x}) \odot \mathbf{h}^i(\mathbf{x})$  with  $\odot$  being the Hadamard product. Gathering features in the spatial domain, these masks’ design is “orthogonal” to the INR model, in which coordinates  $\mathbf{x}$  are handled independently.

For the frequency embedding layer  $\sin(\omega\mathbf{x} + \varphi)$ , masks control the frequencies that participate in the local signal reconstruction process since  $\mathcal{M}^i(\mathbf{x}) \odot \sin(\omega\mathbf{x} + \varphi)$ . Thus, the masks distinguish between low- and high-frequency regions reducing high-frequency interference in smooth areas while enhancing sharp detail reconstruction in edge regions.

For hidden layers, masks adaptively split the domain into different regions and neurons are expressed accordingly. Thus less neurons participate in simple regions, such as background, and almost all neurons contribute to complex patterns, such as edges and textures (see Fig. 3).

### 3.3. Lightweight jointly optimizable masks

We propose to parametrize the mask  $\mathcal{M}$  by a separate network. However, applying masks to every neuron  $h_j^i$  is computationally expensive and may require more parameters. To overcome this, we consider a lightweight, jointly optimizable mask implementation using a multi-scale hash grid network. Its outputs (the masks) are applied to grouped neurons within each network layer, as illustrated in Fig. 2.

**Neuron groups.** During initialization, every neuron in a layer is assigned to a group. For the frequency embedding layer, we group neurons according to their frequency band: low-frequency neurons in the band  $[-\mathcal{L}, \mathcal{L}]$  define a single group, and the high-frequency band  $[-\mathcal{B}, \mathcal{B}] \setminus [-\mathcal{L}, \mathcal{L}]$  is evenly divided into  $n_{band}$  groups. According to Sec. 3.1, each frequency embedding neuron is assigned to the corresponding group by its maximum frequency, *i.e.*,  $\max(|\mathbf{k}|)$ . On the other hand, hidden layers are evenly grouped into neuron groups. The spatially-adaptive group masks (SGMs)  $\mathcal{M}^i(\mathbf{x})$  are then *broadcasted* to all neurons within each neuron group, modulating their outputs.

**Hash grid mask.** The multi-scale hash grid network, introduced by Müller et al. [18] for signal reconstruction, stores features in a hash table and decodes concatenated multi-scale features via an MLP. Here, we consider a hash grid  $\mathcal{H}$  and decoder  $\mathcal{D}$  for representing SGMs. This compact representation enables masks to be jointly optimized with the SNN’s parameters (see Fig. 2). The spatial features of a coordinate  $\mathbf{x}$  are gathered from hash grid vertices (*i.e.*,  $\mathcal{H}(\mathbf{x})$ ) via interpolation and concatenated before being processed by the decoder, that is,  $\mathcal{M}^i(\mathbf{x}) = \mathcal{D}^i \circ \mathcal{H}(\mathbf{x})$ .

Unlike SAPE [8], which gradually “opens” its mask for the first layer neurons, our method allows the network to

optimize masks for different network layers independently from the beginning of training (see [Supp. Sec. 3]).

### 3.4. Training procedure

The SNN and spatially-adaptive masks are jointly optimized, while the frequency embedding layer remains fixed. The loss function consists of the mean squared error (MSE) loss,  $\mathcal{L}_{\text{MSE}}$ , which quantifies the difference between the network’s output and the ground truth signal.

To prevent mask overfitting, we introduce an  $\mathcal{L}_1$  regularization term that encourages mask values to approach discrete Boolean states:

$$\mathcal{L}_1 = \frac{1}{N} \sum_{i,g,\mathbf{x}} \mathcal{M}_g^i(\mathbf{x}),$$

where  $N$  is the number of sampled coordinates. Additionally, we incorporate an optional sparsity regularization term,  $\mathcal{L}_{\text{sparse}}$ , to ensure that at most  $n_{\text{mask}} \in \mathbb{N}$  masks remain active while the others are deactivated:

$$\mathcal{L}_{\text{sparse}} = \sum_{i,\mathbf{x}} \max \left( \sum_g \mathcal{M}_g^i(\mathbf{x}) - n_{\text{mask}}, 0 \right),$$

where  $g$  sums over the groups in layer  $i$ . The final loss function is:  $\mathcal{L} = \mathcal{L}_{\text{MSE}} + \lambda_1 \mathcal{L}_1 + \lambda_{\text{sparse}} \mathcal{L}_{\text{sparse}}$ , where  $\lambda_1$  and  $\lambda_{\text{sparse}}$  control the contributions of the regularization terms.

## 4. Experimental results

We compare SASNet with state-of-the-art INRs with open-source implementations, summarized in Tab. 1. This section is structured as follows: experiment setup and evaluation metrics (Sec. 4.1), quantitative evaluations (Sec. 4.2), and qualitative comparison (Sec. 4.3).

### 4.1. Experiment setup and evaluation metrics

To ensure fair comparison, all INR models are configured with approximately 70,000 trainable parameters, limiting the representation capacity to 8.54 bits per pixel (bpp). Experiments are conducted on the Kodak dataset [1], consisting of 24 lower-resolution images, and the DIV2K [2] validation dataset that contains 100 sharp, complex, and high-resolution images. All images are centrally cropped and resized to  $512 \times 512$  pixels with values in range  $[0, 1]$ . All models are trained for 5,000 steps to achieve convergence, except GaussianImage, which requires 50,000 steps to saturate. Further experimental configurations are given in the supplementary ([Supp. Sec. 3]).

To evaluate fitting accuracy, we use peak signal-to-noise ratio (PSNR) and structural similarity index measure (SSIM) [34]. However, as shown in Fig. 1, these metrics fail to fully capture noisy reconstruction artifacts caused by excessive high-frequency components in INR model, particularly in low-frequency smooth regions. To define these

Methods	PSNR $\uparrow$	SSIM $\uparrow$	PSNR <sub>edge</sub> $\uparrow$	Noisiness $\downarrow$	Act func.	FE.	BC.	Type	bpp
SIREN [32]	32.16	0.90	29.97	0.24 $\pm$ 0.71	sin			Global	8.54
FFN [33]	29.60	0.85	27.18	0.75 $\pm$ 1.99	ReLU	✓		Global	8.77
SAPE [8]	29.86	0.87	27.43	0.30 $\pm$ 1.04	ReLU	✓	✓	Hybrid	8.79
BACON [13]	26.10	0.70	24.30	1.82 $\pm$ 3.81	sin		✓	Global	8.53
WIRE [28]	27.76	0.80	25.47	1.69 $\pm$ 6.06	Gabor wavelet			Local	8.43
FINER [14]	34.05	0.93	31.71	0.43 $\pm$ 1.06	$\sin((1 +  x )x)$			Global	8.54
GaussianImage [38]	33.85	0.94	31.03	-	-			Local	8.50
NeuRBF [4]	31.06	0.88	29.09	0.36 $\pm$ 3.46	ReLU	✓		Hybrid	8.42
SASNet (Ours)	35.52	0.95	33.52	0.16 $\pm$ 0.51	sin	✓	✓	Hybrid	8.34

Table 1. Quantitative evaluation on the DIV2K [2] dataset. In metric columns,  $\uparrow/\downarrow$  indicates that a *higher/lower* numerical value corresponds to better performance. The **best** and **runner-up** values are highlighted in color boxes. For the rest property columns, **Act func.** refers to the main activation function, **FE.** indicates the use of a frequency or positional embedding technique, **BC.** denotes whether the model has an explicit control of the output signal’s band limit, **Type** follows the classification in Sec. 2, and **bpp** represents bits per pixel.

regions, we identify edges by *Canny edge detector* [3] and expand edges by *disk dilation operation*, resulting in a per-pixel binary mask to separate edge and smooth regions, *i.e.*,  $\mathbb{1}_{edge}$  and  $\mathbb{1}_{smooth}$ . Then, to quantitatively measure noise levels, we calculate the difference of the gradient norm between the input image and the model output. Therefore, **noisiness** is defined as:

$$\text{Noisiness} = \mathbb{1}_{smooth} \odot \left| \|\nabla I_{gray}\|_2 - \|\nabla \hat{I}_{gray}\|_2 \right|,$$

and it is measured by *mean* and *standard deviation*. Both the model prediction and the ground truth images are converted to grayscale, denoted as  $\hat{I}_{gray}$  and  $I_{gray}$ . The INR gradient,  $\nabla \hat{I}_{gray}$ , is computed via *automatic differentiation*, while the ground-truth gradient,  $\nabla I_{gray}$ , is estimated using a second-order finite difference method.

On the other hand, the quality of edge-region reconstruction is closely linked to image sharpness. To evaluate this, we compute the edge-region PSNR as:

$$\text{PSNR}_{edge} = -10 \log_{10} (\text{MSE}(\mathbb{1}_{edge} \odot I, \mathbb{1}_{edge} \odot \hat{I})).$$

## 4.2. Quantitative results

We compare SASNet to related INR methods on the DIV2K dataset. Table 1 presents the quantitative comparisons, showing that SASNet outperforms previous works in both PSNR and SSIM, particularly in edge regions. While FINER’s fitting accuracy is better than SIREN, by incorporating higher-frequency components, its global representation increases noisiness. In contrast, SASNet leverages spatially adaptive masks to regulate high frequencies, applying them selectively to relevant regions. This ensures superior accuracy in edge regions while maintaining smoothness elsewhere. Other methods struggle due to either reduced compactness compared to SNNs (*e.g.*, BACON, WIRE, GaussianImage, NeuRBF) or overfitting (*e.g.*, BACON, WIRE, FFN, NeuRBF). Additional quantitative and

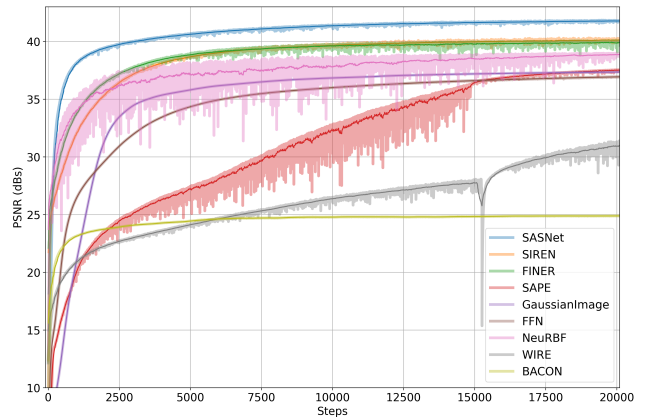


Figure 5. PSNR curves over 20,000 training steps. For each method, the line plot represents the *smoothed metric values*, while the shaded background indicates the actual metric value range during training. WIRE exhibits instability and undergoes two distinct training stages. FFN, SAPE, and NeuRBF utilize unique learning rate schedulers, which differ from other methods that use a fixed learning rate. In contrast, SASNet demonstrates faster convergence, superior fitting accuracy, and more stable training.

qualitative comparisons on DIV2K and Kodak datasets are provided in the supplementary ([Supp. Sec. 4.2]).

Beyond image-fitting quality, model convergence speed and training stability are also crucial. To evaluate these aspects, Fig. 5 presents the PSNR curves of all methods trained over 20,000 steps on a Kodak image, subjecting INRs to prolonged training stress. Among the evaluated methods, SNNs, FFN, and GaussianImage remain stable throughout training, whereas WIRE exhibits instability, undergoing two distinct training phases. SAPE and NeuRBF utilize custom learning rate schedulers, leading to significant training variance. Due to its limited model size and fixed frequency embedding, NeuRBF suffers from overfit-

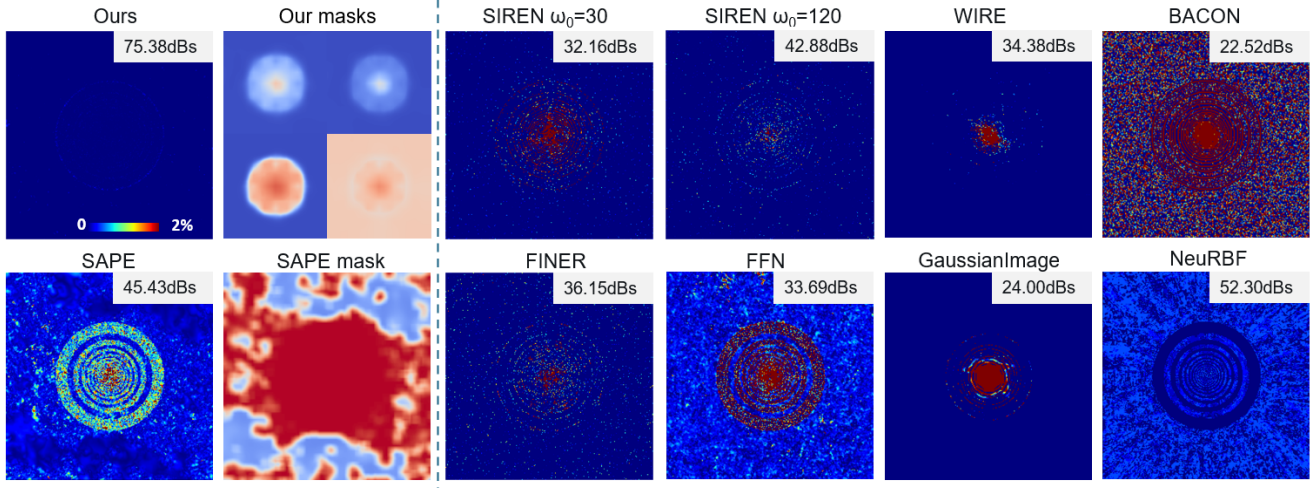


Figure 6. Comparison of toy example fitting by PSNR and error map with shared color encoding as plotted in the first result. Learned masks from SAPE [8] and ours are plotted in the second column. While SAPE has only one mask, our masks for different neuron groups (2 frequency embedding groups (top row) and 2 hidden neuron groups (bottom row)) are selectively plotted.

ting (see Fig. 7) and is less stable. In contrast, SASNet achieves faster convergence than all other methods without requiring a learning rate scheduling strategy, while also maintaining stability throughout the entire training process.

### 4.3. Qualitative results

To evaluate the adaptability of our spatial masks to different frequency distributions, we design a toy example image containing multiple frequency components across different regions, as shown in Fig. 1. This synthetic image is a  $256 \times 256$  binary image, defined as  $\mathbb{1}(\sin(28\pi \exp(d/20)) > 0.5)$ , where  $d$  represents the distance between a pixel and the image center. This example is particularly challenging for SNNs, as it contains numerous sharp edges and a broad range of frequency components, making frequency adaptiveness necessary. This toy example favors local neural representations over global representations since more than half of the image is blank, reducing the fitting complexity for local models. All models are constrained to  $\sim 11,000$  trainable parameters, while all other training hyperparameters remain unchanged. In Fig. 6, we plot each model’s PSNR values alongside their error maps, as error maps provide a clearer visual comparison.

As expected, SIREN’s performance depends on the  $\omega_0$  value. GaussianImage and WIRE struggle to capture high-frequency details near the center, while NeuRBF achieves high PSNR but exhibits overfitting, introducing noise in blank areas. Global methods, particularly FFN and BACON, suffer from under-parameterization, leading to reconstruction errors. Compared to FFN, SAPE mitigates some high-frequency noise in blank areas and improves noise control; however, its mask does not align well with the im-

age’s frequency distribution as shown in the second column.

In contrast, SASNet achieves a significant improvement in PSNR (+32dBs over SIREN) as its jointly optimized multi-frequency masks align effectively with the image’s frequency distribution. This architecture enables accurate sharp edge fitting while minimizing noise in blank areas, demonstrating the effectiveness of adaptive spatial masking.

Besides the toy example, we present a visual comparison of different INRs fitting an image from the Kodak dataset. Overfitting not only increases *noisiness* but also harms the model’s generalization capability. In Fig. 7(a), due to the lack of super-resolution support, we evaluate NeuRBF and GaussianImage by subtly shifting query coordinates ( $1/8$  pixels). The noisy inference result of NeuRBF indicates severe overfitting, while the discrete nature and limited number of Gaussian kernels in GaussianImage lead to special rasterization artifacts. In Fig. 7(b), we analyze two rectangular regions from the input image: one from the background and one from the texture-rich region. Both regions undergo a  $\times 16$  super-resolution, where models are evaluated on a uniform grid of unseen coordinates.

Our spatially-adaptive masks effectively regulate frequency band expressions across different spatial regions. The learned masks align with the complexity of the image, enabling the model to focus its fitting capacity on complex, high-frequency areas while minimizing resource waste and overfitting in smooth regions. Additionally, by applying spatial masks, distinct regions within the image exhibit different frequency band distributions, which reduces network redundancy in SASNet compared to SIREN. Further experimental results and mask visualizations illustrating these effects are provided in the supplementary ([Supp. Fig. 9]).

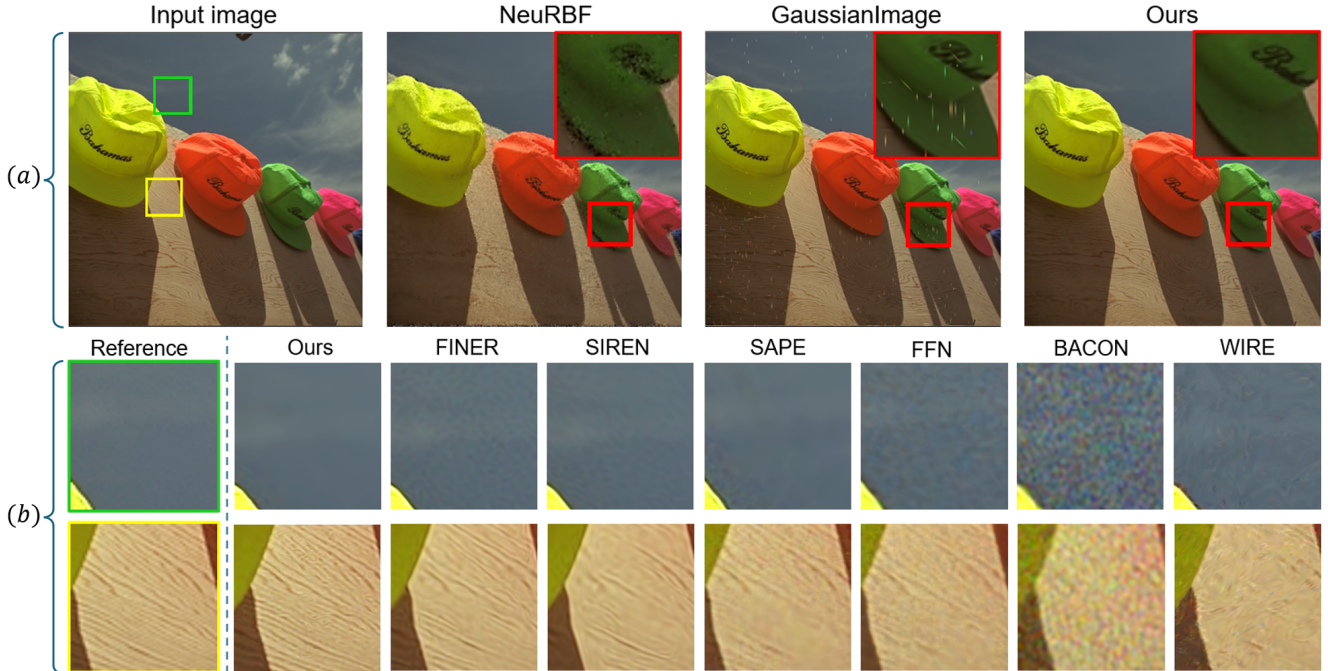


Figure 7. Qualitative comparison by (a) *pixel shifting* and (b) *super-resolution*. In (a), model inference at coordinates with a  $1/8$  pixel shifting in  $x$ - and  $y$ -axis. Green/yellow rectangles highlight the super-resolution regions selected in (b). Red rectangles highlight the zoomed-in plot for better comparison. (b) is the comparison of  $\times 16$  super-resolution inferences for the selected image patches.

#### 4.4. Ablation studies

Our SASNet introduces two key components — the frequency embedding layer and spatially-adaptive masks for neuron groups — to enhance the performance of sinusoidal neural networks (SNNs). In this section, we evaluate the contribution of each module and explore different mask configurations for the network. As summarized in Tab. 2, we start with a baseline SIREN network and incrementally apply the frequency embedding layer (FEmbed.) and masks at different levels: the frequency embedding layer (Freq.), the hidden layers ( $H_1, H_2$ ), or both. While the frequency embedding layer provides the most significant improvement ( $\sim 4$  dB), additional masking strategies further refine reconstruction accuracy ( $\sim 2$  dB gain). Moreover, qualitative enhancements in the details reconstruction and background noise reduction are more noticeable (see [Supp. Sec. 4.5]).

#### 5. Conclusion

We presented **SASNet**, a novel *Spatially-Adaptive Sinusoidal Neural Network*, to address critical challenges in INRs, particularly in SNNs. By incorporating a frequency embedding layer and jointly optimized spatially-adaptive masks, SASNet enhanced frequency localization achieving explicit frequency control, reducing overfitting, and enhancing model compactness. Our results demonstrate that SASNet significantly improves fitting accuracy while reducing

FEmbed.	Masks			PSNR (dBs) $\uparrow$	SSIM $\uparrow$
	Freq.	$H_1$	$H_2$		
				36.00	0.921
✓				39.98	0.953
✓	✓			41.30	0.958
✓	✓	✓		41.44	0.959
✓	✓		✓	41.75	0.963
✓		✓		41.08	0.962
✓			✓	40.56	0.960
	✓	✓	✓	37.10	0.932
✓	✓	✓	✓	<b>42.03</b>	<b>0.966</b>

Table 2. Ablation comparison of our SASNet’s image-fitting accuracy with different modules enabled. **FEmbed.** stands for the usage of the frequency embedding layer. **Masks (L)** stands for enabling masking scheme to the model’s **L** layer.

noise artifacts, outperforming existing INR architectures in both quantitative and qualitative evaluations. In terms of limitations, while SASNet achieves superior results with a compact model, the improvement from a SIREN model might be limited when the model is over-parameterized or the input signal is simple. Future works include exploring SASNet to time-dependent signals, and further improving computational efficiency.

## Acknowledgment

This research was supported by the US National Science Foundation under grant number IIS-1910766, and Google.

## References

- [1] Kodak lossless true color image suite. <http://r0k.us/graphics/kodak/>, 1999. Accessed: 2024-09-01. 5
- [2] Eirikur Agustsson and Radu Timofte. Ntire 2017 challenge on single image super-resolution: Dataset and study. In *Proceedings of the IEEE/CVF Conference on Computer Vision and Pattern Recognition Workshops*, July 2017. 5, 6
- [3] John Canny. A computational approach to edge detection. *IEEE Transactions on Pattern Analysis and Machine Intelligence*, (6):679–698, 1986. 6
- [4] Zhang Chen, Zhong Li, Liangchen Song, Lele Chen, Jingyi Yu, Junsong Yuan, and Yi Xu. Neurf: A neural fields representation with adaptive radial basis functions. In *Proceedings of the IEEE/CVF International Conference on Computer Vision*, pages 4182–4194, 2023. 3, 6
- [5] Amer Essakine, Yanqi Cheng, Chun-Wun Cheng, Lipei Zhang, Zhongying Deng, Lei Zhu, Carola-Bibiane Schönlieb, and Angelica I Aviles-Rivero. Where do we stand with implicit neural representations? a technical and performance survey. *arXiv preprint arXiv:2411.03688*, 2024. 2
- [6] Rizal Fathony, Anit Kumar Sahu, Devin Willmott, and J Zico Kolter. Multiplicative filter networks. In *International Conference on Learning Representations*, 2020. 2
- [7] Haoan Feng, Xin Xu, and Leila De Floriani. Implicitterrain: a continuous surface model for terrain data analysis. In *Proceedings of the IEEE/CVF Conference on Computer Vision and Pattern Recognition Workshop*, pages 899–909, 2024. 1
- [8] Amir Hertz, Or Perel, Raja Giryes, Olga Sorkine-Hornung, and Daniel Cohen-Or. Sape: Spatially-adaptive progressive encoding for neural optimization. *Advances in Neural Information Processing Systems*, 34:8820–8832, 2021. 3, 5, 6, 7
- [9] Chiyu Jiang, Avneesh Sud, Ameesh Makadia, Jingwei Huang, Matthias Nießner, Thomas Funkhouser, et al. Local implicit grid representations for 3d scenes. In *Proceedings of the IEEE/CVF Conference on Computer Vision and Pattern Recognition*, pages 6001–6010, 2020. 1
- [10] Amirhossein Kazerouni, Reza Azad, Alireza Hosseini, Dorit Merhof, and Ulas Bagci. Incode: Implicit neural conditioning with prior knowledge embeddings. In *Proceedings of the IEEE/CVF Winter Conference on Applications of Computer Vision*, pages 1298–1307, 2024. 3
- [11] Bernhard Kerbl, Georgios Kopanas, Thomas Leimkühler, and George Drettakis. 3d gaussian splatting for real-time radiance field rendering. *ACM Transactions on Graphics*, 42(4), July 2023. URL <https://repo-sam.inria.fr/fungraph/3d-gaussian-splatting/>. 3
- [12] Jinseok Kim and Tae-Kyun Kim. Arbitrary-scale image generation and upsampling using latent diffusion model and implicit neural decoder. In *Proceedings of the IEEE/CVF Conference on Computer Vision and Pattern Recognition*, pages 9202–9211, 2024. 1
- [13] David B Lindell, Dave Van Veen, Jeong Joon Park, and Gordon Wetzstein. Bacon: Band-limited coordinate networks for multiscale scene representation. In *Proceedings of the IEEE/CVF Conference on Computer Vision and Pattern Recognition*, pages 16252–16262, 2022. 2, 6
- [14] Zhen Liu, Hao Zhu, Qi Zhang, Jingde Fu, Weibing Deng, Zhan Ma, Yanwen Guo, and Xun Cao. Finer: Flexible spectral-bias tuning in implicit neural representation by variable-periodic activation functions. In *Proceedings of the IEEE/CVF Conference on Computer Vision and Pattern Recognition*, pages 2713–2722, 2024. 3, 6
- [15] Ishit Mehta, Michaël Gharbi, Connelly Barnes, Eli Shechtman, Ravi Ramamoorthi, and Manmohan Chandraker. Modulated periodic activations for generalizable local functional representations. In *Proceedings of the IEEE/CVF International Conference on Computer Vision*, pages 14214–14223, 2021. 3
- [16] Lars Mescheder, Michael Oechsle, Michael Niemeyer, Sebastian Nowozin, and Andreas Geiger. Occupancy networks: Learning 3d reconstruction in function space. In *Proceedings of the IEEE/CVF Conference on Computer Vision and Pattern Recognition*, pages 4460–4470, 2019. 1
- [17] Ben Mildenhall, Pratul P Srinivasan, Matthew Tancik, Jonathan T Barron, Ravi Ramamoorthi, and Ren Ng. Nerf: Representing scenes as neural radiance fields for view synthesis. *Communications of the ACM*, 65(1):99–106, 2021. 1, 3
- [18] Thomas Müller, Alex Evans, Christoph Schied, and Alexander Keller. Instant neural graphics primitives with a multiresolution hash encoding. *ACM Transactions on Graphics*, 41(4):1–15, 2022. 3, 5
- [19] Tiago Novello, Diana Aldana, Andre Araujo, and Luiz Velho. Tuning the frequencies: Robust training for sinusoidal neural networks, 2025. URL <https://arxiv.org/abs/2407.21121>. 3, 4
- [20] Namitha Padmanabhan, Matthew Gwilliam, Pulkit Kumar, Shishira R Maiya, Max Ehrlich, and Abhinav Shrivastava. Explaining the implicit neural canvas: Connecting pixels to neurons by tracing their contributions. In *Proceedings of the IEEE/CVF Conference on Computer Vision and Pattern Recognition*, pages 10957–10967, 2024. 2
- [21] Giambattista Parascandolo, Heikki Huttunen, and Tuomas Virtanen. Taming the waves: sine as activation function in deep neural networks. 2016. 3
- [22] Hallison Paz, Daniel Perazzo, Tiago Novello, Guilherme Schardong, Luiz Schirmer, Vinicius da Silva, Daniel Yukimura, Fabio Chagas, Helio Lopes, and Luiz Velho. Mr-net: Multiresolution sinusoidal neural networks. *Computers & Graphics*, 2023. 4
- [23] Nasim Rahaman, Aristide Baratin, Devansh Arpit, Felix Dräxler, Min Lin, Fred A. Hamprecht, Yoshua Bengio, and Aaron C. Courville. On the spectral bias of neural networks. In *International Conference on Machine Learning*, 2018. 2
- [24] Sameera Ramasinghe and Simon Lucey. Beyond periodicity: Towards a unifying framework for activations in coordinate-

- mlps. In *European Conference on Computer Vision*, pages 142–158. Springer, 2022. 2
- [25] Sameera Ramasinghe, Lachlan E MacDonald, and Simon Lucey. On the frequency-bias of coordinate-mlps. *Advances in Neural Information Processing Systems*, 35:796–809, 2022. 2
- [26] Pradyumna Reddy, Zhifei Zhang, Zhaowen Wang, Matthew Fisher, Hailin Jin, and Niloy Mitra. A multi-implicit neural representation for fonts. *Advances in Neural Information Processing Systems*, 34:12637–12647, 2021. 1
- [27] Vishwanath Saragadam, Jasper Tan, Guha Balakrishnan, Richard G Baraniuk, and Ashok Veeraraghavan. Miner: Multiscale implicit neural representations. In *European Conference on Computer Vision*, 2022. 3
- [28] Vishwanath Saragadam, Daniel LeJeune, Jasper Tan, Guha Balakrishnan, Ashok Veeraraghavan, and Richard G Baraniuk. Wire: Wavelet implicit neural representations. In *Proceedings of the IEEE/CVF Conference on Computer Vision and Pattern Recognition*, pages 18507–18516, 2023. 3, 6
- [29] Hemanth Saratchandran, Sameera Ramasinghe, Violetta Shevchenko, Alexander Long, and Simon Lucey. A sampling theory perspective on activations for implicit neural representations. *arXiv preprint arXiv:2402.05427*, 2024. 2, 3
- [30] Kexuan Shi, Xingyu Zhou, and Shuhang Gu. Improved implicit neural representation with fourier reparameterized training. In *Proceedings of the IEEE/CVF Conference on Computer Vision and Pattern Recognition*, pages 25985–25994, 2024. 3
- [31] Vincent Sitzmann, Michael Zollhöfer, and Gordon Wetzstein. Scene representation networks: Continuous 3d-structure-aware neural scene representations. *Advances in Neural Information Processing Systems*, 32, 2019. 1
- [32] Vincent Sitzmann, Julien Martel, Alexander Bergman, David Lindell, and Gordon Wetzstein. Implicit neural representations with periodic activation functions. *Advances in Neural Information Processing Systems*, 33:7462–7473, 2020. 1, 2, 3, 4, 6
- [33] Matthew Tancik, Pratul Srinivasan, Ben Mildenhall, Sara Fridovich-Keil, Nithin Raghavan, Utkarsh Singhal, Ravi Ramamoorthi, Jonathan Barron, and Ren Ng. Fourier features let networks learn high frequency functions in low dimensional domains. *Advances in Neural Information Processing Systems*, 33:7537–7547, 2020. 2, 3, 6
- [34] Zhou Wang, Alan C Bovik, Hamid R Sheikh, and Eero P Simoncelli. Image quality assessment: from error visibility to structural similarity. *IEEE Transactions on Image Processing*, 13(4):600–612, 2004. 5
- [35] Yiheng Xie, Towaki Takikawa, Shunsuke Saito, Or Litany, Shiqin Yan, Numair Khan, Federico Tombari, James Tompkin, Vincent Sitzmann, and Srinath Sridhar. Neural fields in visual computing and beyond. *Computer Graphics Forum*, 41(2):641–676, 2022. doi: <https://doi.org/10.1111/cgf.14505>. 1
- [36] Gizem Yüce, Guillermo Ortiz-Jiménez, Beril Besbinar, and Pascal Frossard. A structured dictionary perspective on implicit neural representations. In *Proceedings of the IEEE/CVF Conference on Computer Vision and Pattern Recognition*, pages 19228–19238, 2022. 4
- [37] Andreas Zell, Nuri Benbarka, Timon Hofer, and Hamd Ul Moqueet Riaz. Seeing implicit neural representations as fourier series. In *Proceedings of the IEEE/CVF Winter Conference on Applications of Computer Vision*. IEEE Computer Society, 2022. 4
- [38] Xinjie Zhang, Xingtong Ge, Tongda Xu, Dailan He, Yan Wang, Hongwei Qin, Guo Lu, Jing Geng, and Jun Zhang. Gaussianimage: 1000 fps image representation and compression by 2d gaussian splatting. In *European Conference on Computer Vision*, 2024. 3, 6
- [39] Yunxiang Zhang, Alexandr Kuznetsov, Akshay Jindal, Kenneth Chen, Anton Sochenov, Anton Kaplanyan, and Qi Sun. Image-gs: Content-adaptive image representation via 2d gaussians. *arXiv preprint arXiv:2407.01866*, 2024. 3

# SASNet: Spatially-Adaptive Sinusoidal Neural Networks - Supplementary Material -

Haoan Feng<sup>1</sup>, Diana Aldana<sup>2</sup>, Tiago Novello<sup>2</sup>, Leila De Florian<sup>1</sup>  
<sup>1</sup>University of Maryland, College Park, <sup>2</sup> IMPA

hfengac@umd.edu, diana.aldana@impa.br,  
 tiago.novello@impa.br, deflo@umd.edu

## Contents

<b>1. Proof of Theorem 1</b>	<b>1</b>
<b>2. Contribution map</b>	<b>2</b>
<b>3. Implementation details</b>	<b>2</b>
<b>4. More experimental results</b>	<b>3</b>
4.1. Influence of the hyperparameter $\omega_0$ . . . . .	3
4.2. Experiments on Kodak and DIV2K datasets . . . . .	3
4.3. Additional experiments on CT medical images . . . . .	3
4.4. Additional experiments on FFHQ dataset . . . . .	4
4.5. Additional ablation study results . . . . .	4
<b>5. Extreme cases</b>	<b>4</b>

## 1. Proof of Theorem 1

In the main paper we claim that the  $j$ -th neuron of the  $i + 1$ -th layer  $h_j^{i+1}$  has the following expansion:

$$h_j^{i+1}(\mathbf{x}) = \sum_{\mathbf{k} \in \mathbb{Z}} \alpha \sin(\langle \mathbf{k}, \mathbf{y} \rangle + b_j^{i+1}) \quad (1)$$

where  $\mathbf{y} = \mathbf{W}^i \mathbf{h}^i(\mathbf{x}) + \mathbf{b}^i$  and  $\alpha = \prod_l J_{k_l}(W_{j_l}^{i+1})$  is the product of Bessel functions of the first kind at the  $j$ -th row of the hidden matrix  $\mathbf{W}^{i+1}$ .

Considering  $h_j^{i+1} = \sin(\sum_{k=1}^m W_{jk}^{i+1} \sin(y_k) + b_j^{i+1})$ , we now prove Eq. 1 via induction over  $m$ . For  $m = 1$ ,

$$\begin{aligned} h_j^{i+1} &= \sin(W_{j1}^{i+1} \sin(y_1) + b_j^{i+1}) \\ &= \sin(W_{j1}^{i+1} \sin(y_1)) \cos(b_j^{i+1}) + \\ &\quad \cos(W_{j1}^{i+1} \sin(y_1)) \sin(b_j^{i+1}) \end{aligned}$$

$$\begin{aligned} &= \sum_{k \in \mathbb{Z} \text{ odd}} J_k(W_{j1}^{i+1}) \sin(ky_1) \cos(b_j^{i+1}) + \\ &\quad \sum_{k \in \mathbb{Z} \text{ even}} J_k(W_{j1}^{i+1}) \cos(ky_1) \sin(b_j^{i+1}) \\ &= \sum_{k \in \mathbb{Z} \text{ odd}} J_k(W_{j1}^{i+1}) \sin(ky_1 + b_j^{i+1}) + \\ &\quad \sum_{k \in \mathbb{Z} \text{ even}} J_k(W_{j1}^{i+1}) \sin(ky_1 + b_j^{i+1}) \\ &= \sum_{k \in \mathbb{Z}} \alpha \sin(ky_1 + b_j^{i+1}) \end{aligned}$$

The first equality comes from the trigonometrical equation  $\sin(a + b) = \sin(a) \cos(b) + \cos(a) \sin(b)$ , the second one is derived from a property of Bessel functions of the first kind (see [2, p. 361]). For the third equality, we use the properties  $\sin(a) \cos(b) = \frac{\sin(a+b) + \sin(a-b)}{2}$  and  $J_{-k}(a) = (-1)^k J_k(a)$  to rewrite the summations. Now, suppose Eq. 1 holds for  $m - 1$ . Then,

$$\begin{aligned} h_j^{i+1} &= \sin\left(\sum_{k=1}^m W_{jk}^{i+1} \sin(y_k) + b_j^{i+1}\right) \\ &= \sin\left(\sum_{k=1}^{m-1} W_{jk}^{i+1} \sin(y_k) + b_j^{i+1}\right) \cos\left(W_{jm}^{i+1} \sin(y_m)\right) + \\ &\quad \cos\left(\sum_{k=1}^{m-1} W_{jk}^{i+1} \sin(y_k) + b_j^{i+1}\right) \sin\left(W_{jm}^{i+1} \sin(y_m)\right) \\ &= \sum_{\substack{\mathbf{k} \in \mathbb{Z}^{m-1} \\ l \in \mathbb{Z} \text{ even}}} \alpha_{\mathbf{k}} J_l(W_{jm}^{i+1}) \sin\left(\sum_{s=1}^{m-1} k_s y_s + b_j^{i+1}\right) \cos(l y_m) + \\ &\quad \sum_{\substack{\mathbf{k} \in \mathbb{Z}^{m-1} \\ l \in \mathbb{Z} \text{ odd}}} \alpha_{\mathbf{k}} J_l(W_{jm}^{i+1}) \cos\left(\sum_{s=1}^{m-1} k_s y_s + b_j^{i+1}\right) \sin(l y_m) \\ &= \sum_{\mathbf{k} \in \mathbb{Z}^m} \alpha \sin(\langle \mathbf{k}, \mathbf{y} \rangle + b_j^{i+1}) \end{aligned}$$

Once again, the second equality comes from the sum of angles property for sines and the third one uses the induction hypothesis.

## 2. Contribution map

Analyzing the contribution of each neuron is an effective approach to understand a network’s fitting capability and parameter redundancy. According to Padmanabhan et al. [9], for a neuron  $h_j^i$ , its contribution to each pixel coordinate  $\mathbf{x}$  is defined by a mapping from its weights  $\mathbf{W}_j^i$  to the neuron output scalar  $h_j^i(\mathbf{x})$ , i.e.,  $\sum_l h_j^i(\mathbf{x}) \cdot \mathbf{W}_{jl}^{i+1}$ . Thus, the contribution map of  $h_j^i$  can be obtained by accumulating the pixel-wise contribution across the entire image. Contribution maps illustrate the spatial representation focus of neurons<sup>1</sup>.

In the main paper, Fig. 3 presents contribution maps of nine neurons from SIREN [11], WIRE [10], and SASNet, representing different INR categories: *Global*, *Local*, and *Hybrid* (see more examples in the Related work). The maps reveal that neurons in *global* INRs tend to be redundant and “*space-agnostic*”, whereas those in *local* INRs exhibit sparser and more spatially localized contributions. Additionally, the global nature of INRs gives rise to model overfitting - neurons fitting high-frequency regions introduce noise into low-frequency areas. In such regions, e.g., image backgrounds, other neurons may need to counteract the effect of high-frequency noise by learning complementary signals to suppress these artifacts. This inefficiency in INRs is one of the main issues addressed in this paper.

## 3. Implementation details

In the quantitative experiment section, we follow each method’s open-source implementation (unless specifically mentioned below). To make a fair comparison, we modify their network widths and learning rates to guarantee the final fitting result is close to their network capacity. For sinusoidal networks, we increase the value of hyperparameter  $\omega$  from 30 to 43 because the input images are of higher resolution than those in the previous paper and this  $\omega$  value makes a good balance between PSNR fitting accuracy and image noisiness. Here are some implementation details:

- SIREN [11]: 3 hidden layers of width 185 neurons. The learning rate is fixed to  $1e-4$ .
- FINER [8]: 3 hidden layers of width 185 neurons. The learning rate is fixed to  $1e-4$ . After comparing different initializations of biases, we decided not to change the scale of the biases and only kept the activation function so that it reached a fitting accuracy and the training process was more stable.

- BACON [7]: 3 hidden layers of width 128 neurons. The learning rate is fixed to  $5e-3$ .
- FFN [12] and SAPE [5]: we use the implementation in SAPE [5]<sup>2</sup>. For each training step, instead of sampling coordinates, we fed all coordinates for supervision. 3 hidden layers of width 100 neurons. The learning rate is fixed to  $1e-4$ . The number of frequencies is set to 256 based on experiments on the Kodak dataset [1].
- WIRE [10]: we use the implementation that each network layer is using a complex Gabor function (except the output layer). 3 hidden layers of width 106 complex neurons. The learning rate is fixed to  $5e-4$ . For the image-fitting task, the hyperparameter  $\omega$  is set to 20, and the  $\sigma$  is set to 30, as suggested by its implementation. For the toy example, the hyperparameter  $\omega$  is set to 4, and the  $\sigma$  is set to 10 by hyperparameter search.
- GaussianImage [13]: without applying quantization, we fitted each image with 8700 Gaussian kernels for 50000 training iterations.
- NeuRBF [4]: we use their official implementation except for reducing the number of initial RBF kernels to reduce the number of trainable parameters.

For our SASNet, the frequency embedding layer is of width 400 neurons, and two hidden layers are of width 116 neurons. To initialize the frequency embedding layer, half neurons are initialized for the low-frequency range  $[-12, 12]$  by random sampling. The rest of the neurons are initialized by sampling the high-frequency range limited by the preset band limit of 60. High-frequency neurons are further split into 5 even-width frequency bands.

We assume that low-frequency components are essential for smooth implicit function reconstruction across the entire spatial domain. Therefore, the low-frequency band mask is set to *one* and fixed throughout training. The remaining masks are initialized around 0.5, following the standard random initialization of the hash grid and MLP decoder. For each hidden layer, neurons are evenly split into 8 neuron groups. For spatially-adaptive masks, a multi-scale hash grid is constructed with 10 levels and 2 hidden features on each grid vertex. Interpolated features are concatenated and fed into one ReLU-based MLP decoder with 1 hidden layer of width 48 for simplicity. The learning rate of the SNN branch is fixed to  $1e-4$ , while the learning rates of the hash grid and the decoder are set to  $5e-4$ .

For BACON and SASNet, the initialization of the frequency embedding layer ensures the fitted image is periodic. However, this periodic output may lead to drastic changes in border pixels and affect the accuracy of gradient calculation. Therefore, we apply a simple but effective solution: during training, each coordinate is multiplied by an

<sup>1</sup>Publicly available at <https://github.com/namithap10/xinc>

<sup>2</sup>Publicly available at <https://github.com/amirhertz/SAPE>.

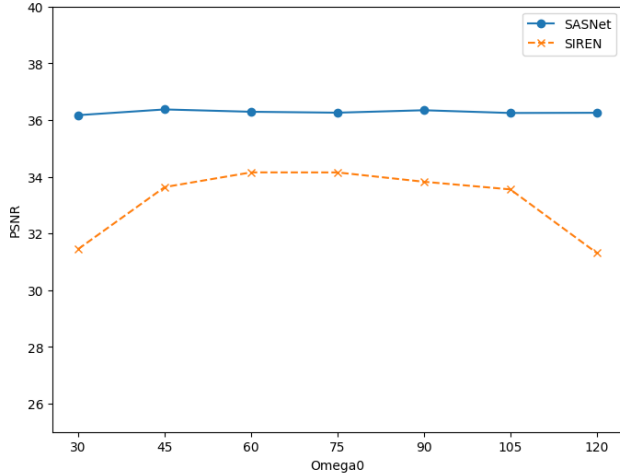


Figure 1. Sensitivity comparison between SIREN and our SASNet to the change of hyperparameter  $\omega_0$ .

extra scalar value of 0.95 to leave a margin on each border of the image. During the experiment, we found this implementation effectively improves the reconstruction quality on the image border.

## 4. More experimental results

### 4.1. Influence of the hyperparameter $\omega_0$

As shown in Fig. 1 of the main paper, SIREN [11] is highly sensitive to the choice of the hyperparameter  $\omega_0$ , making its selection non-trivial. Smaller values lead to blurry reconstructions without introducing high-frequency noise, whereas higher values reduce spectral bias and produce sharper outputs, but resulting in increased noisiness in smooth regions.

In contrast, SASNet leverages spatially-adaptive masks to separate frequency band expressions, preventing high-frequency neuron outputs from propagating into smooth regions. As a result, the choice of  $\omega_0$  has minimal impact on the final reconstruction accuracy, as illustrated in Fig. 1, where PSNR remains stable across different  $\omega_0$  values.

### 4.2. Experiments on Kodak and DIV2K datasets

In this section, more experimental results are provided: (1) Tab. 1 provides the quantitative evaluation results on the Kodak dataset; (2) Fig. 2 and Fig. 3 are line plot of PSNR curve for each image and the PSNR statistic for each method in both datasets; (3) Fig. 4 and Fig. 5 plot more visual comparison results for the Kodak and DIV2K datasets.

### 4.3. Additional experiments on CT medical images

In addition to the two RGB image datasets used in the main paper, we further compare SASNet with FINER [8]

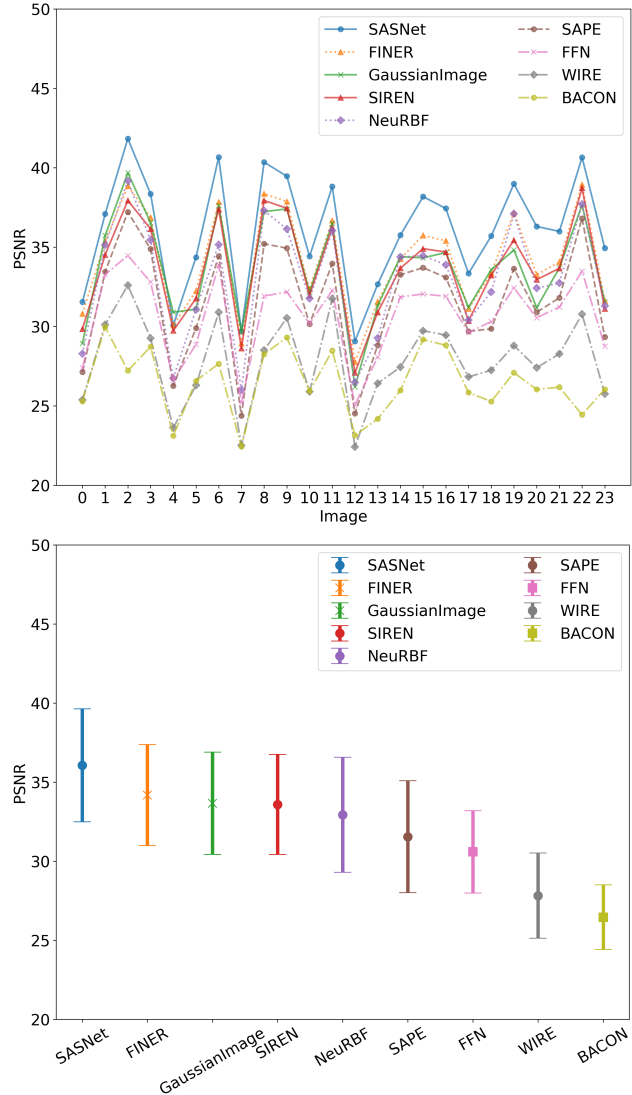


Figure 2. PSNR curve and statistics for the Kodak dataset.

and SIREN [11] on a publicly available CT medical image dataset<sup>3</sup>, which contains 100 CT scan images from the TCIA cancer imaging archive [3]. Each scan has a resolution of  $512 \times 512$  and consists of a single-channel grayscale image, normalized to  $[0, 1]$ . We conduct the image-fitting experiments using the same configuration as in the main paper without any modifications.

Table 2 presents the quantitative evaluations, showing that SASNet achieves higher fitting accuracy, particularly in preserving edge details. Notably, for single-channel images, the model configuration used in previous experiments is sufficiently large for all methods to fit the data without overfitting. Consequently, the noisiness across all methods

<sup>3</sup><https://www.kaggle.com/datasets/kmader/siim-medical-images>

Methods	PSNR $\uparrow$	SSIM $\uparrow$	PSNR <sub>edge</sub> $\uparrow$	Noisiness $\downarrow$	Act func.	FE.	BC.	Type	bpp
SIREN [11]	33.60	0.91	30.68	0.41 $\pm$ 1.09	sin			Global	8.54
FFN [12]	30.60	0.83	27.42	0.94 $\pm$ 2.40	ReLU	✓		Global	8.77
SAPE [5]	31.56	0.85	28.97	0.54 $\pm$ 1.44	ReLU	✓	✓	Hybrid	8.79
BACON [7]	26.47	0.66	23.70	1.90 $\pm$ 3.73	sin		✓	Global	8.53
WIRE [10]	27.83	0.75	24.53	2.22 $\pm$ 7.92	Gabor wavelet			Local	8.43
FINER [8]	34.19	0.91	31.62	0.52 $\pm$ 1.24	sin((1 +  x )x)			Global	8.54
GaussianImage [13]	33.67	0.92	30.39	-	-			Local	8.50
NeuRBF [4]	32.98	0.87	31.33	0.83 $\pm$ 4.85	ReLU	✓		Hybrid	8.42
SASNet (Ours)	36.08	0.93	34.66	0.42 $\pm$ 1.11	sin	✓	✓	Hybrid	8.34

Table 1. Quantitative evaluation on the Kodak [1] dataset. **Type** and **bpp** denotes the property of each method. For other metrics,  $\uparrow/\downarrow$  indicates the numerical value is *higher/lower* the method performs better. The **best** and **runner-up** values are highlighted in color boxes. Summarization of state-of-the-art neural representations. **Act func.** is abbr for the activation function. **FE.** is abbr for frequency or positional embedding. **BC.** denotes if the model has an explicit control mechanism for the reconstructed signal’s band limit.

remains low. This is further observable in Fig. 6, where both the model outputs and their error maps are visualized.

#### 4.4. Additional experiments on FFHQ dataset

The Flickr-Faces-HQ (FFHQ) dataset [6] contains a large collection of high-quality human face images at a resolution of  $1024 \times 1024$ . For this experiment, 100 images are randomly selected from the training image set. Similar to the medical image experiment, the same network configuration is applied to SIREN [11], FINER [8], and our SASNet.

Table 3 presents the quantitative evaluations, while Fig. 7 provides a visual comparison among these methods. SASNet achieves higher fitting accuracy (as observed in the error maps), and this PSNR improvement does not result in an increased noisiness level, in contrast to FINER.

#### 4.5. Additional ablation study results

In the main paper, we conduct an ablation study to evaluate the contribution of each module, namely the frequency embedding layer and spatially-adaptive masks at different layers. Figure 8 presents a visual comparison among SIREN, SASNet with only frequency embedding (without masks), and the full SASNet. The results demonstrate that while the frequency embedding layer enhances fitting accuracy, particularly for sharper reconstructions, it also introduces additional noise in the image background. By applying spatially-adaptive masks, the quality of background reconstruction significantly improves, as indicated by the reduction in image gradient intensity.

Figure 9 visualizes the jointly optimized spatial masks of SASNet and SAPE for the same input image as in Fig. 8. The learned masks for different frequency bands effectively align with the spatial complexity of the image, enabling the model to focus its fitting capacity on complex, high-frequency regions while preventing resource waste and overfitting in simpler regions.

Additionally, a hidden mask is selected from each hidden layer, and contribution maps of the corresponding neuron groups are visualized. These results indicate that spatial masks allow different regions to encode distinct frequency bands, leading to lower network redundancy in SASNet compared to SIREN. In smooth and easy-to-fit regions, only a subset of neurons contributes to reconstruction, whereas in complex, texture-rich regions, most neurons participate in signal reconstruction, demonstrating the effectiveness of spatially-adaptive frequency control.

### 5. Extreme cases

In Figure Fig. 3, we observe that in certain DIV2K images, INR methods struggle to achieve optimal performance, while GaussianImage attains a higher PSNR value. To further analyze this phenomenon, we present two extreme cases in Fig. 10, illustrating the relationship between INR performance and image content. Both images primarily consist of high-frequency repeated patterns that span almost the entire domain, and with minimal pixel variation within each “color strip”. This structure is particularly well-suited for GaussianImage, as each Gaussian kernel can efficiently cover a larger portion of the domain with minimal computational effort. Conversely, INR methods suffer from spectral bias and an insufficient number of parameters to effectively capture such a broad frequency spectrum, leading to reduced fitting accuracy in these scenarios.

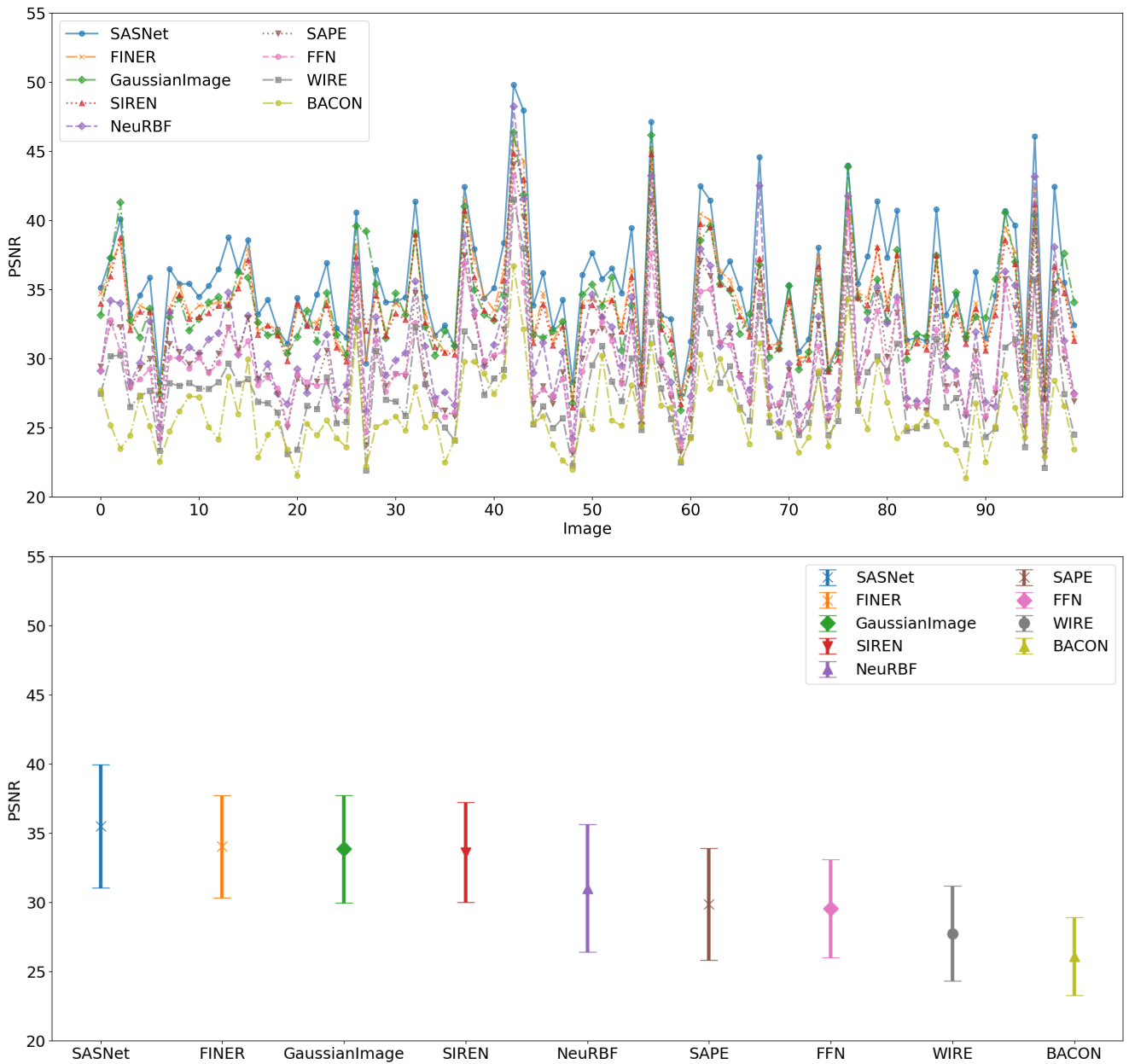


Figure 3. PSNR curve and statistics for the DIV2K dataset.

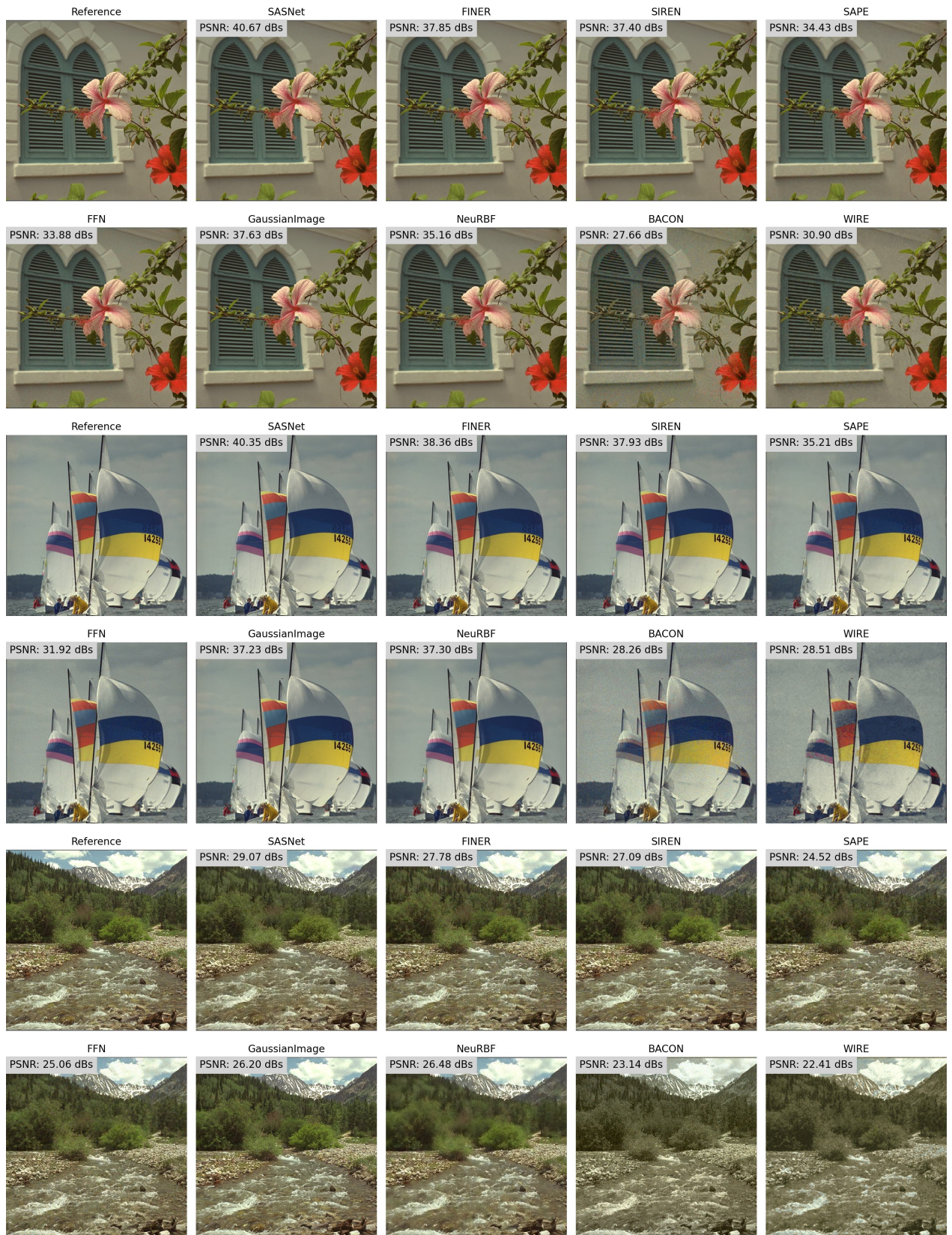


Figure 4. Visual comparison on the Kodak dataset. PSNR values are annotated in the upper-left corner of each image.

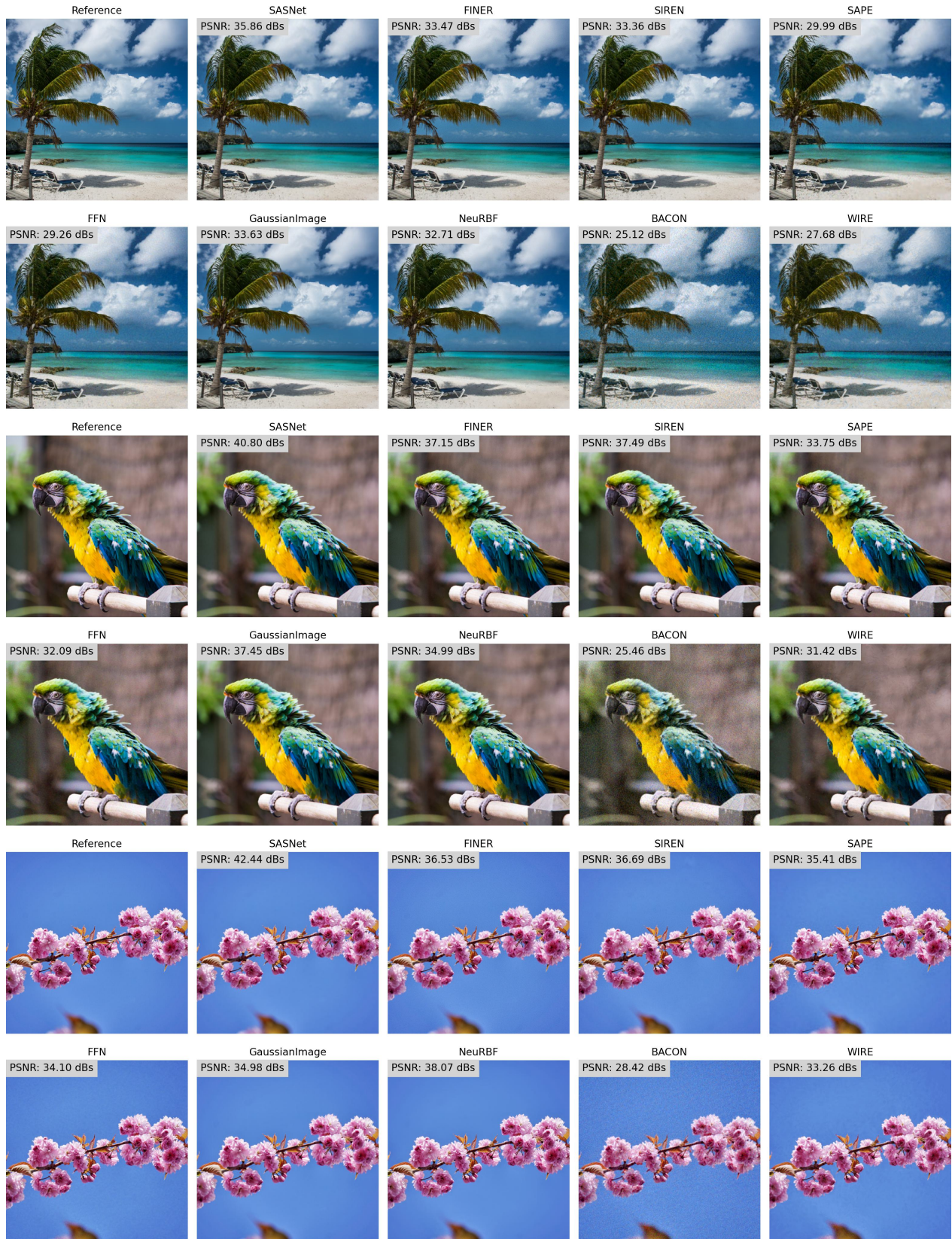


Figure 5. Visual comparison on the DIV2K dataset. PSNR values are annotated in the upper-left corner of each image.

Methods	PSNR $\uparrow$	SSIM $\uparrow$	PSNR <sub>edge</sub> $\uparrow$	Noisiness $\downarrow$
SIREN [11]	47.07	0.98	42.94	0.35 $\pm$ 0.54
FINER [8]	48.49	0.99	45.56	0.35 $\pm$ 0.55
SASNet (Ours)	50.21	0.99	49.58	0.37 $\pm$ 0.65

Table 2. Quantitative evaluation on a medical image dataset. For each metric,  $\uparrow/\downarrow$  indicates the numerical value is *higher/lower* the method performs better.

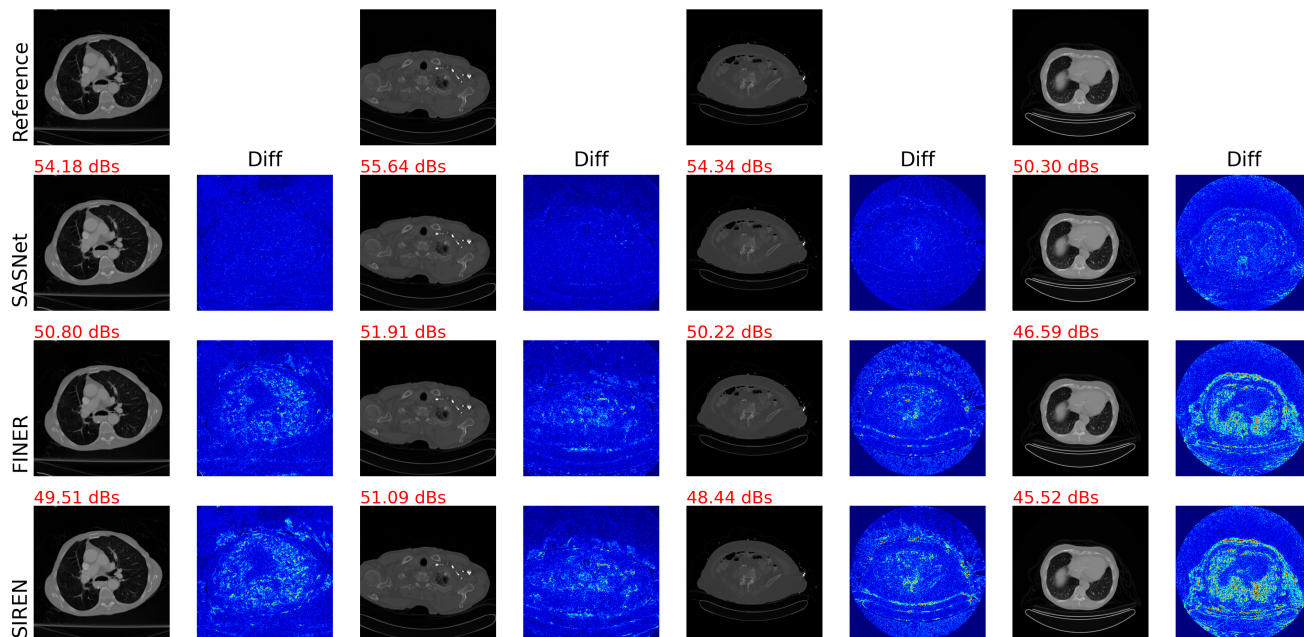


Figure 6. Medical CT scans’ fitting results by SASNet, FINER, and SIREN. For each of the four examples, PSNR values are annotated on the upper left corner of model outputs. Besides each model’s output image, the *Diff* column shows the error map with a *jet* color encoding (up to 2% absolute difference).

## References

- [1] Kodak lossless true color image suite. <http://r0k.us/graphics/kodak/>, 1999. Accessed: 2024-09-01. 2, 4
- [2] Milton Abramowitz and Irene A Stegun. *Handbook of mathematical functions with formulas, graphs, and mathematical tables*, volume 55. US Government printing office, 1948. 1
- [3] Brad Albertina, Mark Watson, Chandra Holback, Rose Jarosz, Shanah Kirk, Yueh Lee, Kimberly Rieger-Christ, and John Lemmerman. The cancer genome atlas lung adenocarcinoma collection (tcga-luad). 2016. 3
- [4] Zhang Chen, Zhong Li, Liangchen Song, Lele Chen, Jingyi Yu, Junsong Yuan, and Yi Xu. Neurbf: A neural fields representation with adaptive radial basis functions. In *Proceedings of the IEEE/CVF International Conference on Computer Vision*, pages 4182–4194, 2023. 2, 4
- [5] Amir Hertz, Or Perel, Raja Giryes, Olga Sorkine-Hornung, and Daniel Cohen-Or. Sape: Spatially-adaptive progressive encoding for neural optimization. *Advances in Neural Information Processing Systems*, 34:8820–8832, 2021. 2, 4
- [6] Tero Karras, Samuli Laine, and Timo Aila. A style-based generator architecture for generative adversarial networks. In *Proceedings of the IEEE/CVF conference on computer vision and pattern recognition*, pages 4401–4410, 2019. 4
- [7] David B Lindell, Dave Van Veen, Jeong Joon Park, and Gordon Wetzstein. Bacon: Band-limited coordinate networks for multiscale scene representation. In *Proceedings of the IEEE/CVF Conference on Computer Vision and Pattern Recognition*, pages 16252–16262, 2022. 2, 4
- [8] Zhen Liu, Hao Zhu, Qi Zhang, Jingde Fu, Weibing Deng, Zhan Ma, Yanwen Guo, and Xun Cao. Finer: Flexible spectral-bias tuning in implicit neural representation by variable-periodic activation functions. In *Proceedings of the IEEE/CVF Conference on Computer Vision and Pattern Recognition*, pages 2713–2722, 2024. 2, 3, 4, 8, 9
- [9] Namitha Padmanabhan, Matthew Gwilliam, Pulkit Kumar, Shishira R Maiya, Max Ehrlich, and Abhinav Shrivastava. Explaining the implicit neural canvas: Connecting pixels to neurons by tracing their contributions. In *Proceedings of*

Methods	PSNR $\uparrow$	SSIM $\uparrow$	PSNR <sub>edge</sub> $\uparrow$	Noisiness $\downarrow$
SIREN [11]	37.58	0.95	34.20	0.42 $\pm$ 0.82
FINER [8]	38.16	0.95	35.09	0.50 $\pm$ 0.90
SASNet (Ours)	39.69	0.95	37.64	0.43 $\pm$ 0.85

Table 3. Quantitative evaluation on the FFHQ dataset. For each metric,  $\uparrow/\downarrow$  indicates the numerical value is *higher/lower* the method performs better.

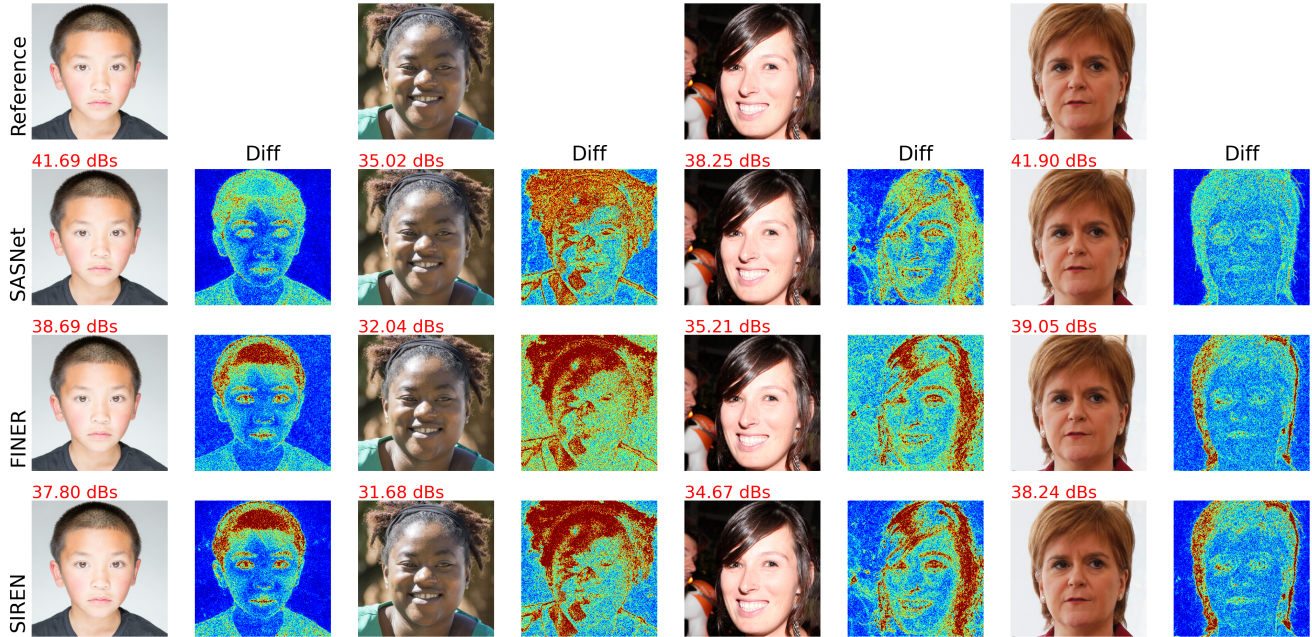


Figure 7. Fitting results of FFHQ human faces SASNet, FINER, and SIREN. For each of the four examples, PSNR values are annotated on the upper left corner of model outputs. Besides each model’s output image, the *Diff* column shows the error map with a *jet* color encoding (up to 2% absolute difference).

*the IEEE/CVF Conference on Computer Vision and Pattern Recognition*, pages 10957–10967, 2024. 2

- [10] Vishwanath Saragadam, Daniel LeJeune, Jasper Tan, Guha Balakrishnan, Ashok Veeraraghavan, and Richard G Baraniuk. Wire: Wavelet implicit neural representations. In *Proceedings of the IEEE/CVF Conference on Computer Vision and Pattern Recognition*, pages 18507–18516, 2023. 2, 4
- [11] Vincent Sitzmann, Julien Martel, Alexander Bergman, David Lindell, and Gordon Wetzstein. Implicit neural representations with periodic activation functions. *Advances in Neural Information Processing Systems*, 33:7462–7473, 2020. 2, 3, 4, 8, 9
- [12] Matthew Tancik, Pratul Srinivasan, Ben Mildenhall, Sara Fridovich-Keil, Nithin Raghavan, Utkarsh Singhal, Ravi Ramamoorthi, Jonathan Barron, and Ren Ng. Fourier features let networks learn high frequency functions in low dimensional domains. *Advances in Neural Information Processing Systems*, 33:7537–7547, 2020. 2, 4
- [13] Xinjie Zhang, Xingtong Ge, Tongda Xu, Dailan He, Yan Wang, Hongwei Qin, Guo Lu, Jing Geng, and Jun Zhang.

Gaussianimage: 1000 fps image representation and compression by 2d gaussian splatting. In *European Conference on Computer Vision*, 2024. 2, 4

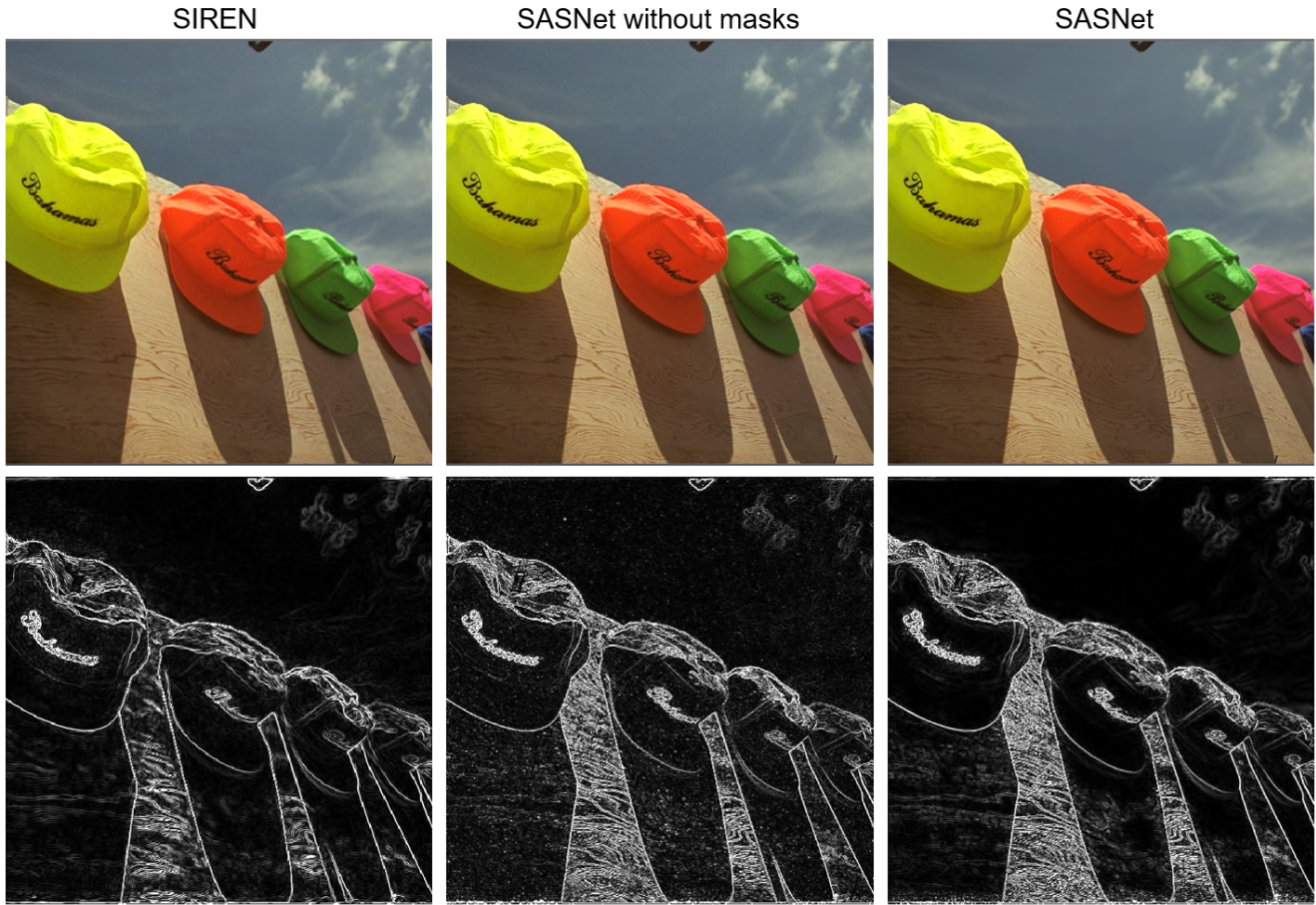


Figure 8. Visual comparison between SIREN, SASNet without masks, and full SASNet. First row shows the image reconstructed and the second row shows the corresponding gradient intensity obtained by network automatic differentiation (*autograd* in PyTorch).

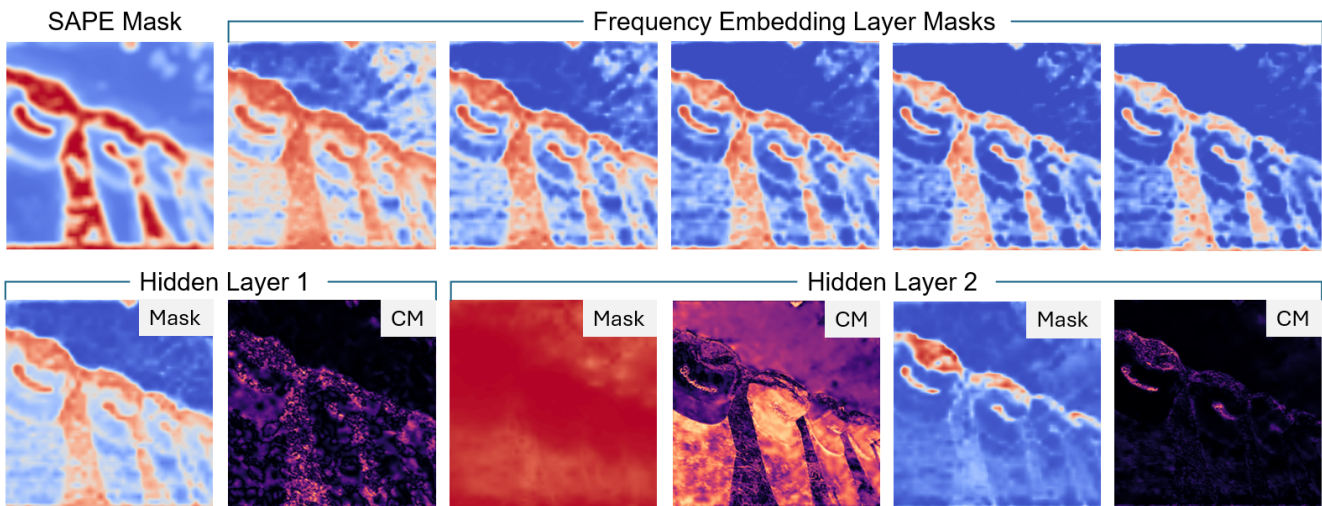


Figure 9. SAPE mask and our masks of the image-fitting task in Figure Fig. 9. **CM**: contribution map. The first hidden layer mask shows that this group has a global contribution as also shown in the CM. However, some details on edges and texture regions can be missed, and therefore the other group focuses only on these small regions.

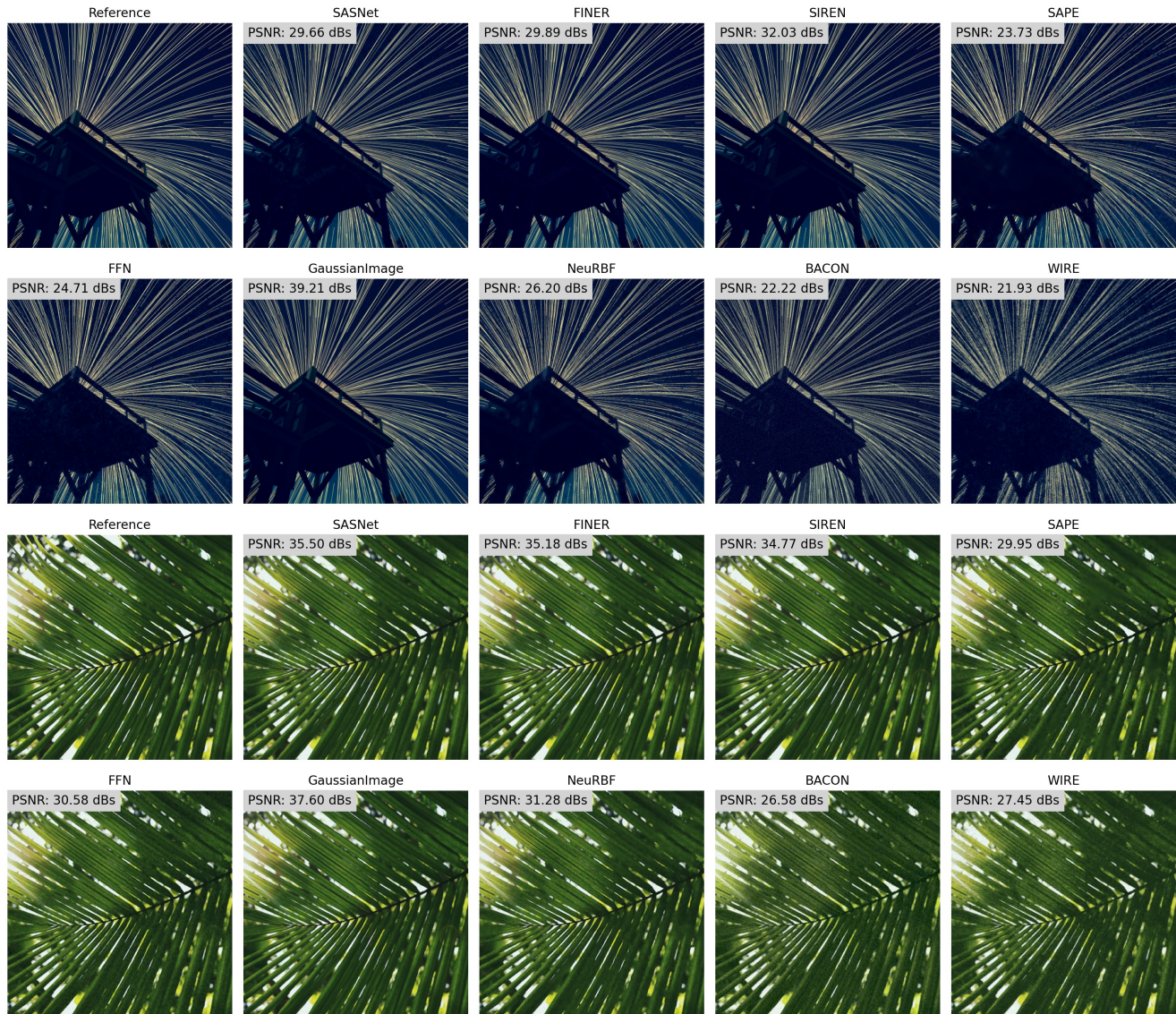


Figure 10. Example images from the DIV2K dataset showing when performances of INRs are limited. Both images are of complex signal components and higher frequencies than others, and contain hard edges covering almost the whole domain.